

Safe MPC Alignment with Human Directional Feedback

Zhixian Xie, Wenlong Zhang, Yi Ren, Zhaoran Wang, George J. Pappas, Wanxin Jin

Abstract—In safety-critical robot planning or control, manually specifying safety constraints or learning them from demonstrations can be challenging. In this article, we propose a certifiable alignment method for a robot to learn a safety constraint in its model predictive control (MPC) policy from human online directional feedback. To our knowledge, it is the first method to learn safety constraints from human feedback. The proposed method is based on an empirical observation: human directional feedback, when available, tends to guide the robot toward safer regions. The method only requires the direction of human feedback to update the learning hypothesis space. It is certifiable, providing an upper bound on the total number of human feedback in the case of successful learning, or declaring the hypothesis misspecification, i.e., the true safety constraint cannot be found within the specified hypothesis space. We evaluated the proposed method in numerical examples and user studies with two simulation games. Additionally, we tested the proposed method on a real-world Franka robot arm performing mobile water-pouring tasks. The results demonstrate the efficacy and efficiency of our method, showing that it enables a robot to successfully learn safety constraints with a small handful (tens) of human directional corrections.

Index Terms—Learning from Human Feedback, Constraint Inference, Model Predictive Control, Human-Robot Interaction.

I. INTRODUCTION

In robot policy design, safety is always the top priority, especially in safety-critical applications, such as robots operating near humans, where safety violations can lead to irreversible losses. While extensive work in safe control [1] and reinforcement learning [2] focuses on deducing robot policy given safety constraints, less attention has been paid to how to specify the safety constraints in the first place. In many applications, specifying proper safety constraints can be challenging. First, *explicit boundary for safe robot behavior can be hard to model*. For example, when delivering food

Zhixian Xie and Wanxin Jin are with the Intelligent Robotics and Interactive Systems (IRIS) Lab in the School for Engineering of Matter, Transport and Energy at Arizona State University. Wanxin Jin is the corresponding author. Emails: zxxie@asu.edu and wanxinjin@gmail.com.

Wenlong Zhang is with the Polytechnic School at Arizona State University. Email: wenlong.zhang@asu.edu.

Yi Ren is with the School for Engineering of Matter, Transport and Energy at Arizona State University. Email: yiren@asu.edu.

Zhaoran Wang is with the Departments of Industrial Engineering & Management Sciences, Northwestern University. Email: zhaoranwang@gmail.com.

George J. Pappas is with the Department of Electrical and Systems Engineering at the University of Pennsylvania. Email: pappsg@seas.upenn.edu.

This work involved human subjects or animals in its research. Approval of all ethical and experimental procedures and protocols was granted by ASU's Institutional Review Board under Application No. STUDY00020060, and performed in the line with Title 45 of the Code of Federal Regulations, Part 46 (45 CFR 46).

We acknowledge the funding support from ABRC grant RFGA2024-022-013.

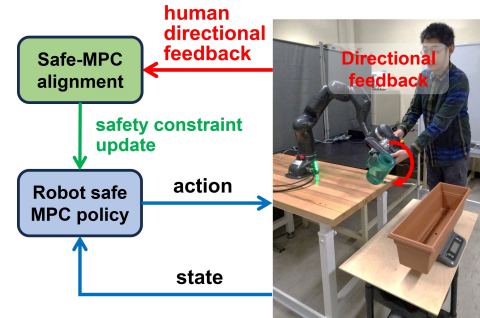


Fig. 1. Illustration of the proposed safe MPC alignment. Our method online updates the safety constraint using human directional feedback, such that the robot eventually aligns the safe MPC policy with human intent for the safety-critical task.

in a crowded restaurant, a service robot must balance a tray to avoid spills; this requires constraints on robot speed, food weight distributions, and interaction with its surroundings, all of which can be complex to model. Second, *user's perception of safety may vary*. In the same example, some diner may feel secure with the robot staying within a foot when delivering, while others may feel uncomfortable with such proximity.

The challenges in safety specification lead to two questions. Q1: can a robot learn safety constraints to align with human intent in an *interactive* manner? Q2: can such a learning process be *user-data efficient*? Recent work [3]–[5] explored learning safety constraints from human demonstrations. However, acquiring safety-informative demonstrations could be difficult. Learning from human preference [6]–[12] offers a new paradigm, where a user's preference of one trajectory over the other is used for robot learning. The preference, however, can be difficult for a human to make, especially in early learning stages. [13]–[19] proposed learning from human physical corrections. While promising, [20] suggests those methods are potentially sensitive to correction magnitude: corrections can lead to overshooting and inefficiency of learning. All those feedback-driven learning methods primarily focus on learning rewards instead of safety constraints.

This paper aims to answer the previous two questions by proposing a new paradigm for a robot to efficiently learn safety constraints in its model predictive control (MPC) policy from human feedback. We name the method *safe MPC alignment*. As in Fig. 1, a user, observing the robot's potentially unsafe behavior, provides online corrections to the robot. Upon receiving human corrections, the robot immediately updates the safety constraints in its MPC policy and continues with the updated policy. Our method only requires/utilizes *direction* of a human correction [20]. For example, when a human user

corrects an autonomous car, he/she only needs to give the command of ‘turn left’ or ‘turn right’, without dictating how much the car needs to turn. Directional corrections permit a consistently large and flexible correction space. Importantly, the proposed method guarantees the exponential convergence with finite rounds of human corrections, or outputs failure with certified hypothesis misspecification. Specifically, we highlight our main contributions below.

(I) We propose the method of *safe MPC alignment* from human directional correction. It enables a robot to learn a safe MPC policy from online human directional corrections. To our knowledge, it is the first work for interactive learning of safety constraints from human feedback.

(II) We show that *safe MPC alignment* is certifiable: it guarantees exponential convergence with a finite number of human corrections and enables verification when the true safety constraint falls outside the specified hypothesis space.

(III) Extensive user studies have been conducted to validate the proposed method, including a real-world experiment on the Franka robot arm. The results show the effectiveness and efficiency of our method.

The remaining paper is organized as follows. Section II reviews the related work, and Section III formulates the safe MPC alignment problem. The main method is presented in Section IV. Section V gives the implementation details and the main results. Sections VI-VIII provide the experiments and user studies. Discussions and Conclusions are in Section IX.

II. RELATED WORK

A. Learning from Demonstrations

Under the general theme of learning from human inputs, the proposed method falls into the category of learning from demonstrations, where costs/rewards are learned from expert data using inverse reinforcement learning (IRL) [21]. IRL methods typically run offline: human demonstrations are first collected, and then reward/cost is learned [21]–[26]. As pointed by [27], acquiring demonstration data can be difficult in practice, due to either the high degrees of freedom of a robot, or the lack of knowledge about the desired robot behavior [28].

In this work, we focus on interactive learning of safety constraints. Different from learning from demonstrations, the proposed method only requires a user to incrementally improve the current robot motion by providing directional feedback.

B. Learning from Human Feedback

This line typically focuses on learning rewards/costs from human feedback in forms of preferences and corrections. Human preference is typically given as user’s ranking of two or multiple robot trajectories [6]–[12], which is modeled using the Bradley-Terry formulation [29]. Human corrections require a user to intervene and correct the robot at runtime, from which a intended reward/cost can be inferred. Human corrections can include language command [30]–[34] and physical corrections [13], [15], [18]. Since human corrections can be sparse in time, many methods [13]–[19] use trajectory deformation methods to interpolate sparse corrections as a continuous trajectory. Some strategies are further proposed to deal with learning robustness

and uncertainty, such as updating one feature at a time [15] or formulating the problem in the Kalman Filter framework [14].

Our work belongs to the category of learning from human corrections. But instead of learning rewards/costs, we focus on learning safety constraints from human corrections, which has not been addressed before. Methodologically, we propose a certifiable method, which guarantees the learning convergence with finite human corrections, and certifies the hypothesis misspecification. Those results are missing in existing methods.

C. Learning Constraints from Demonstrations

An increasing number of work focuses on learning safety constraints from demonstrations. One straightforward idea is to cast the problem as a binary classification. [3], [35] consider the trajectories of lower cost as the unsafe samples. [36] proposes adjusting the constraints toward decreasing the safety margin of feasible policies. Safety constraints can also be learned via mixed integer programming [3], [35], pessimistic adjustment [36], and no-regret algorithm [37]. Those methods typically require collecting negative (unsafe) samples, which can be challenging in real robot systems. Another line of work attempts to learn safety constraints only from safe demonstration. For example, [38]–[40] infer the safety constraints by exploiting the optimality conditions of demonstrations. Different probabilistic formulations are also used, such as maximum likelihood [5], [41], [42], causal entropy [43], [44], and Bayesian inference [45], [46]. Among them, safety constraints can be represented as a set of safe states [38], the belief of constraints [39], Gaussian process [40], or a convex hull in policy space [4].

Using demonstrations, the vast majority of the above methods formulate the constraint learning in offline settings, and the learning process usually involves repetitive policy optimization. Those methods can be difficult to be deployed online, where a robot is expected to quickly update its safety estimate and respond to human feedback. To fill this gap, we will develop the first method, to our best knowledge, to enable online learning of safe constraints from human feedback.

III. PRELIMINARY AND PROBLEM FORMULATION

A. Safe Model Predictive Control

Consider a robot equipped with a safe model predictive control (Safe MPC) policy defined below, where the safety constraint is learnable and parameterized by $\theta \in \mathbb{R}^r$.

$$\begin{aligned} \min_{\mathbf{u}_{0:T-1}} \quad & J(\mathbf{u}_{0:T-1}; \mathbf{x}_0) = \sum_{t=0}^{T-1} c(\mathbf{x}_t, \mathbf{u}_t) + h(\mathbf{x}_T) \\ \text{subject to} \quad & \mathbf{x}_{t+1} = \mathbf{f}(\mathbf{x}_t, \mathbf{u}_t) \quad \text{given } \mathbf{x}_0 \\ & g_{\theta}(\mathbf{x}_{0:T}, \mathbf{u}_{0:T-1}) \leq 0 \end{aligned} \quad (1)$$

Here, $\mathbf{x}_t \in \mathbb{R}^n$ and $\mathbf{u}_t \in \mathbb{R}^m$ are robot state and action, respectively; $t = 0, 1, 2, \dots, T$ is the time step over a short prediction horizon T , starting from a given \mathbf{x}_0 . Define $\mathbf{x}_{0:T} = (\mathbf{x}_0, \mathbf{x}_1, \dots, \mathbf{x}_T)$ and $\mathbf{u}_{0:T-1} = (\mathbf{u}_0, \mathbf{u}_1, \dots, \mathbf{u}_{T-1})$; $J(\cdot)$ is the given cost function including the running cost $c(\cdot)$ and final cost $h(\cdot)$; $\mathbf{f}(\cdot, \cdot)$ is the system dynamics; $g_{\theta}(\cdot)$ is the safety constraint parameterized by $\theta \in \mathbb{R}^r$. Given starting state \mathbf{x}_0 and parameter θ , the optimal plan (solution) to (1), denoted as $\xi_{\theta} = \{\mathbf{u}_{0:T-1}^{\theta}, \mathbf{x}_{0:T}^{\theta}\}$, is an implicit function of θ .

In a receding horizon implementation, \mathbf{x}_0 is set as the real robot's current state (estimation) $\mathbf{x}_k^{\text{real}}$, where $k = 0, 1, 2, \dots$, is the global rollout time step of the Safe MPC policy. Only the first action \mathbf{u}_0^θ in each ξ_θ is applied to the robot to move the robot to the next state $\mathbf{x}_{k+1}^{\text{real}}$. This process repeats at each rollout time step $k = 0, 1, \dots$. Such a receding horizon implementation leads to a closed-loop policy, denoted as π_θ , mapping from robot current state $\mathbf{x}_k^{\text{real}}$ to its action \mathbf{u}_0^θ .

B. Safe Asymptotic Approximation of Safe MPC

We present a penalty-based approximation to the Safe MPC in (1). Define trajectory variable $\xi = \{\mathbf{u}_{0:T-1}, \mathbf{x}_{0:T}\}$ and the following penalty objective:

$$B(\xi, \theta) = J(\xi) - \gamma \ln(-g_\theta(\xi)). \quad (2)$$

Here, $B(\xi, \theta)$ includes the cost $J(\xi)$ and safety constraint $g_\theta(\xi)$ in a logarithmic barrier transformation. $\gamma > 0$ is the barrier parameter, controlling the weight of safety penalty $-\ln(-g_\theta(\xi))$ relative the cost. With $B(\xi, \theta)$, one can establish the following penalty-based MPC

$$\min_{\mathbf{u}_{0:T-1}} B(\xi, \theta) \quad \text{subject to} \quad \mathbf{x}_{t+1} = \mathbf{f}(\mathbf{x}_t, \mathbf{u}_t). \quad (3)$$

We denote the optimal plan to (3) as $\xi_\theta^\gamma = \{\mathbf{u}_{0:T-1}^{\theta, \gamma}, \mathbf{x}_{0:T}^{\theta, \gamma}\}$. The following result from [47] states the penalty-based MPC (3) is an asymptotic, safe approximation to Safe MPC (1).

Lemma 1. (Theorem 2 in [47]) *If the Safe MPC (1) satisfies certain mild conditions (i.e., local second-order condition and strict complementarity), then for any small $\gamma > 0$, the penalty-based MPC (3) has a (local) solution ξ_θ^γ , and ξ_θ^γ is safe with respect to the original constraint, i.e., $g_\theta(\xi_\theta^\gamma) < 0$, and ξ_θ^γ satisfies the first-order condition of (3). Furthermore, ξ_θ^γ is asymptotically approximate ξ_θ : $\xi_\theta^\gamma \rightarrow \xi_\theta$ as $\gamma \rightarrow 0$.*

The above lemma asserts that solving the Safe MPC (1) can be replaced by solving penalty-based MPC (3). The solution approximation is controlled by γ for arbitrary accuracy: $\xi_\theta^\gamma \rightarrow \xi_\theta$ as $\gamma \rightarrow 0$. A good approximation is achieved by a smaller γ . On the contrary, if γ is larger, penalty-based MPC will lead to more safety-conservative solution ξ_θ^γ . In the development below, we fix the parameter γ in (3). We denote the penalty-based MPC policy in (3) as π_θ^γ .

C. Problem Formulation

1) *Representation of Human Intended Safety:* Consider a human is supervising the robot's behavior. In Safe MPC (1), we hypothesize that user-intended safety can be represented by a subset of the trajectory space:

$$\mathcal{S}(\theta_H) = \{(\mathbf{x}_{0:T}, \mathbf{u}_{0:T-1}) \mid g_{\theta_H}(\mathbf{x}_{0:T}, \mathbf{u}_{0:T-1}) \leq 0\}. \quad (4)$$

Here, θ_H is from a set $\Theta_H \in \Theta_H$, encoding all possible user intended safety. Θ_H is implicit and unknown to the robot. For the robot policy π_θ^γ , if $\theta \in \Theta_H$, the user considers the planned robot motion to be safe; otherwise if $\theta \notin \Theta_H$, the robot motion by π_θ^γ might not be safe at certain time. We use an implicit set $\Theta_H \in \mathbb{R}^r$, instead of a single point θ_H , to capture the potential variance of user intents. We suppose that a volume measure of Θ_H , $\text{Vol}(\Theta_H)$, is non-zero, and a user intent $\theta_H \in \Theta_H$ can vary at different steps and contexts, but always within Θ_H .

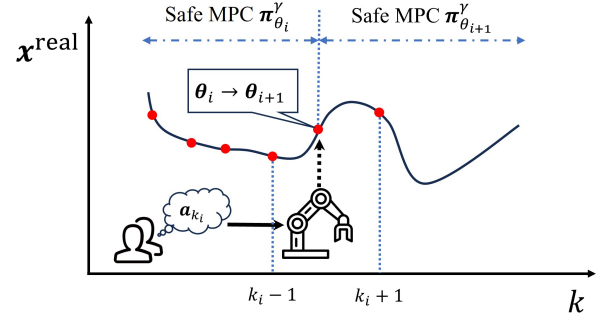


Fig. 2. Update of Safe MPC policy with human directional corrections.

2) *Human Directional Correction:* As shown in Fig. 2, we consider human correcting a robot online while the robot is executing π_θ^γ . Specifically, let i be the index of learning update, and suppose robot current policy is $\pi_{\theta_i}^\gamma$. During rollout of $\pi_{\theta_i}^\gamma$, the robot receives a human correction $\mathbf{a}_{k_i} \in \mathbb{R}^m$ at the rollout time step k_i . Here, we do not pose any assumption on correction time k_i and its duration due to the sparsity or intermittency of human feedback. In other words, the human can apply one or multiple corrections at any time as necessary. But we assume human correction \mathbf{a}_{k_i} is in the robot action space. For example, in autonomous driving where the robot action space is steering angle and acceleration, human can directly apply feedback with the steering wheel and pedals. In some other applications, the action space correction can be achieved via a specific user interface. For example, to correct a torque-controlled robot arm, human's correction on the end-effector can be mapped into joint torque via the Jacobian transpose. The reason why we only consider the action space correction is because first, corrections in input spaces may be easier to implement, as shown in our later experiments, and second, corrections in state spaces can be infeasible for the under-actuated robot system.

After receiving a human correction \mathbf{a}_{k_i} , the robot updates the safety parameter $\theta_i \rightarrow \theta_{i+1}$ in (1) for its Safe MPC. Then, the robot continues with $\pi_{\theta_{i+1}}^\gamma$ until the next possible user correction. This process repeats until the convergence of the policy update or the user is satisfied with the robot's motion.

While the correction \mathbf{a} given by human is real-valued, only its direction is used in the learning process. This means that we will use the sign (for scalar signal) or its normalized unit vector (for vector-valued correction signal) for learning update. The magnitude of the correction is NOT taken into account in the learning process. As we will show later, directional feedback provides a consistently large and flexible correction space, effectively overcoming the over-shooting correction, compared to magnitude feedback.

3) *Robot Operation Safety and Emergency Stop:* In the aforementioned learning procedure, the robot will respond to human correction by executing the updated safe MPC policy π_θ^γ . However, it is possible that the robot may still exit the user-intended safety. In such cases, the human may trigger an emergency stop to stop the robot and potentially restart it from a desired safety region. In such case, the executed motion before the emergency stop is assumed safe. In other words, until an emergency stop is triggered, human correction

typically occur when the robot is still in the intended safety set; otherwise, the correction would be useless. For instance, correcting a vehicle after it is crashed is futile.

4) *Parametric Safety Constraints:* In (4), the safety set is defined as a zero sublevel set of g_θ . If g_θ has sufficient representation power, the safety set can represent a complex safety region. In the following, we focus on a weighted-features parameterization of g_θ , which has been commonly used by the prior work on learning cost/reward [4], [20], [48]–[50]. Specifically,

$$g_\theta(\xi) = \phi_0(\xi) + \theta_1\phi_1(\xi) + \theta_2\phi_2(\xi) + \dots + \theta_r\phi_r(\xi), \quad (5)$$

with $\theta = [\theta_1, \theta_2, \dots, \theta_r]^\top \in \mathbb{R}^r$ and $\phi = [\phi_1, \phi_2, \dots, \phi_r]^\top$ the learnable weight and feature vectors, respectively. We fix the weight of ϕ_0 as unit, because otherwise, θ has scaling ambiguity, i.e., any scaled $c \cdot \theta$ with $c > 0$ lead to the same constraint. In this work, we assume that the features in ϕ are given a priori. These features, defined in system states (e.g., position, velocity) and actions, can be either manually defined or obtained from pre-trained neural representations, leveraging prior knowledge of the environment and tasks, as demonstrated in our experiments. The feature selection itself is beyond the scope of this paper and is left for future work. A more detailed discussion of this assumption and its limitations is in Section IX-A3.

5) *Problem of Safe MPC Alignment:* Following the procedure of human correction and robot policy update in Section III-C, we aim to develop a policy update rule: $\theta_i \rightarrow \theta_{i+1}$ for each received human correction, such that $\theta_i \rightarrow \theta_H \in \Theta_H$, as $i = 1, 2, 3, \dots$, i.e., safety constraints in the robot's safe MPC policy will be aligned with human intent.

IV. OVERVIEW OF SAFE MPC ALIGNMENT

A. Hypothesis on Human Directional Corrections

Informally, we have the following intuitions on human feedback. First, human corrections, on average, improve the robot's safety. Second, human correction is typically proactive and happens before the robot leaves the human-intended safety set. In other words, human correction is made when the robot is still in $\mathcal{S}(\theta_H)$ in (4). For example, it is useless to correct a vehicle after its crash. Third, human feedback is typically safety-margin aware: as a robot approaches the safety boundary, human users tend to prioritize safety over the task cost. For instance, when a vehicle moves closer to obstacles, humans may instinctively shift their focus to avoiding collisions rather than pursuing the original target. In the following, we will formalize those intuitions.

Without loss of generality, suppose the motion plan ξ_θ^γ is a local solution to the penalty MPC (3), and when the robot execute the first action $\mathbf{u}_0^{\theta, \gamma}$ (receding horizon implementation), a human applies a directional correction \mathbf{a} in robot action space. In this subsection, the subscription k_i is omitted for notation simplicity. Define

$$\mathbf{a} = (\mathbf{a}^\top, 0, 0, \dots) \in \mathbb{R}^{mT}. \quad (6)$$

We assume there is a nonzero volume set $\bar{\Theta}_H$ (containing a ball) in user implicit set Θ_H , i.e., $\bar{\Theta}_H \subseteq \Theta_H$, such that for

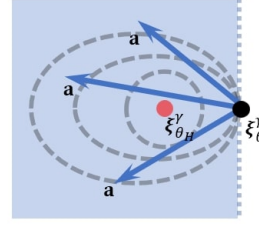


Fig. 3. Illustration of directional correction in the space of robot plan ξ . The grey circles represent the level contours of $B(\xi, \theta_H)$. The black dot stands for the current motion plan ξ_θ^γ and the red point stands for optimal plan ξ_θ^H with θ_H . The blue region stands for the half-space of all possible human correction under our assumption (7). Some samples of human corrections are shown by blue arrows.

any $\theta_H \in \bar{\Theta}_H$, the human correction \mathbf{a} , on average, indicates a direction of lowering the penalty value $B(\xi_\theta^\gamma, \theta_H)$. Concretely, it means \mathbf{a} on averages points in the direction of the negative gradient of $B(\xi, \theta_H)$ at ξ_θ^γ , i.e.,

$$\forall \theta_H \in \bar{\Theta}_H, \mathbb{E}_\mathbf{a} \langle \mathbf{a}, -\nabla B(\xi_\theta^\gamma, \theta_H) \rangle = \langle \bar{\mathbf{a}}, -\nabla B(\xi_\theta^\gamma, \theta_H) \rangle \geq 0. \quad (7)$$

Here, $\langle \cdot, \cdot \rangle$ denotes the inner product operation, and $\mathbb{E}_\mathbf{a}(\mathbf{a}) = \bar{\mathbf{a}}$ denotes the expectation value of \mathbf{a} . $\nabla B(\xi, \theta)$ denotes the full gradient of B with respect to $\mathbf{u}_{0:T-1}$ evaluated at trajectory $\xi = \{\mathbf{u}_{0:T-1}, \mathbf{x}_{0:T}\}$. Similar notations apply to J and g below. Since $\nabla B(\xi, \theta)$ is not dependent on \mathbf{a} , the expectation can be moved inside the inner product. Because state sequence $\mathbf{x}_{0:T}$ is the rollout of $\mathbf{u}_{0:T-1}$ on dynamics, the differentiation goes through the dynamics equation.

Equation (7) shows that although the human correction \mathbf{a} is provided as a real-valued vector, only its direction—not its magnitude—affects the inequality. This brings one advantage of directional correction compared to the magnitude-based correction: the allowable human correction satisfying (7) always account for half of the action space, making directional corrections more accessible for human users, as shown in Fig. 3. Recall that $B(\xi, \theta) = J(\xi) - \gamma \ln(-g_\theta(\xi))$, by extension of the gradient, (7) becomes

$$\forall \theta_H \in \bar{\Theta}_H, \langle \bar{\mathbf{a}}, -\nabla J(\xi_\theta^\gamma) \rangle + \gamma \frac{1}{-g_{\theta_H}(\xi_\theta^\gamma)} \langle \bar{\mathbf{a}}, -\nabla g_{\theta_H}(\xi_\theta^\gamma) \rangle \geq 0. \quad (8)$$

For the above equation, we have the following interpretations.

(I) The first and second terms of (8) correspond to human correction toward lowering the cost and improving the safety of ξ_θ^γ , respectively. γ weighs between two improvements.

(II) If we interpret the value of $-g_{\theta_H}(\xi_\theta^\gamma)$ as the safety margin of the plan ξ_θ^γ , (8) suggests that the human correction is safety-margin aware: the closer the robot motion get to the unsafe region, the more will human improve the robot safety than minimizing the cost. This property is consistent with our previous intuition.

(III) (7) implies $B(\xi_\theta^\gamma, \theta_H)$ is well-defined in the first place:

$$\forall \theta_H \in \bar{\Theta}_H, g_{\theta_H}(\xi_\theta^\gamma) < 0. \quad (9)$$

This corresponds to the third intuition: a user typically gives correction only when the robot is in user intended safety region.

In sum, the two constraints (7) and (9) formalize the intuitions we have observed at the beginning of this subsection. Those constraints will be used in the robot learning next.

B. Main Algorithm: Learning by Hypothesis Space Cutting

To find $\theta_H \in \bar{\Theta}_H \subseteq \Theta$ for the Safe MPC, our idea is that for each human correction $i = 0, 1, 2, \dots$, the robot performs one learning iteration, by updating a hypothesis space $\Theta_i \in \mathbb{R}^r$, a set containing all possible $\bar{\Theta}_H$. Initially, the robot may choose a large box hypothesis space Θ_0 :

$$\Theta_0 = \{\theta \mid c_l \leq \theta \leq c_u\} \subset \mathbb{R}^r, \quad (10)$$

in which c_l, c_u are the vectors of lower and upper bounds of the box space, respectively, and the inequalities are applied element-wise. By saying a Θ_0 large enough, we assume

$$\bar{\Theta}_H \subset \Theta_0. \quad (11)$$

Later, we will show our method can self-access the misspecification, where (11) is not met.

Recall the procedure of human correction in Section III-C and Fig. 2. At i -th learning update, $i = 1, 2, 3, \dots$, the robot executes $\pi_{\theta_i}^\gamma$ with $\theta_i \in \Theta_{i-1}$. The user gives a correction \mathbf{a}_{k_i} at rollout step k_i . By letting $\bar{\mathbf{a}}_i = (\mathbf{a}_{k_i}^T, 0, 0, \dots)$ as in (6), we can establish the following two constraints from the previous hypotheses (7) and (9):

$$\mathcal{C}_i = \{\theta \mid \langle \bar{\mathbf{a}}_i, \nabla B(\xi_{\theta_i}^\gamma, \theta) \rangle \leq 0, \quad g_\theta(\xi_{\theta_i}^\gamma) < 0\}, \quad (12)$$

which we refer to as the *cutting set*. Using \mathcal{C}_i , one can update the hypothesis space

$$\Theta_i = \Theta_{i-1} \cap \mathcal{C}_i. \quad (13)$$

The above update can be viewed as using (12) to cut the hypothesis space Θ_{i-1} to remove portions where $\bar{\Theta}_H$ is impossible. The new hypothesis space Θ_i will be used for the next iteration. With the above update, we have the following result.

Lemma 2. *Given $\bar{\Theta}_H \subset \Theta_0$, if one follows the update (13), then $\bar{\Theta}_H \subset \Theta_i$ for all $i = 1, 2, 3, \dots$*

Proof. See the proof in Appendix A-A. \square

As in Fig. 4, the procedure of robot learning is to cut and move the hypothesis space based on human directional correction. Therefore, we name our learning method *Safe MPC Alignment by Hypothesis Space Cutting*. As a summary, we present the three main steps of our algorithm below.

Safe MPC Alignment by Hypothesis Space Cutting

Initialize Θ_0 that contains $\bar{\Theta}_H$. Repeat the following three steps for $i = 1, 2, \dots, K$ until $\theta_i \in \bar{\Theta}_H$.

Step 1: Robot chooses parameter $\theta_i \in \Theta_{i-1}$ for its current Safe MPC $\pi_{\theta_i}^\gamma$.

Step 2: Human user applies a directional correction \mathbf{a}_{k_i} while robot executes $\pi_{\theta_i}^\gamma$.

Step 3: Perform hypothesis space cut using (13) to get new hypothesis space Θ_i .

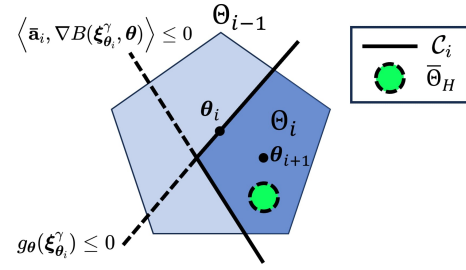


Fig. 4. The update of hypothesis space (2D example). Two cutting lines are used to cut Θ_{i-1} to Θ_i . The user intent set $\bar{\Theta}_H$ is contained in Θ_i . New θ_{i+1} is chosen from Θ_i for the updated Safe MPC policy.

At i th learning update, the robot chooses $\theta_i \in \Theta_{i-1}$ for its current Safe MPC $\pi_{\theta_i}^\gamma$. While executing $\pi_{\theta_i}^\gamma$, the robot receives human correction \mathbf{a}_{k_i} at the rollout time step k_i . This correction leads to a cutting set \mathcal{C}_i (12), which will update Θ_{i-1} to Θ_i in (13). The above iteration repeats $i = 1, 2, 3, \dots$. From (13), one can easily see that $\Theta_0 \supseteq \Theta_1 \supseteq \dots \supseteq \bar{\Theta}_H$. Given a volume measure, it follows $\text{Vol } \Theta_0 \geq \text{Vol } \Theta_1 \geq \dots \geq \text{Vol } \bar{\Theta}_H$. Thus, the volume of the hypothesis space is at least not increasing after each correction. It is hoped that the volume of the hypothesis space decreases quickly, such that new θ_{i+1} increases its chance of choosing from $\bar{\Theta}_H$ — meaning a successful safety alignment between the robot and human.

For the *Safe MPC Alignment*, we will later (Section V) show within finite number K of correction, the method will either

- (I) surely have $\theta_i \in \bar{\Theta}_H \subset \Theta_H$, $i < K$, or
 - (II) declare the failure due to misspecification ($\bar{\Theta}_H \cap \Theta_0 = \emptyset$)
- Also in Section V, we will provide implementation details for the above hypothesis space cutting procedure.

C. Properties and Geometric Interpretations

We next show properties and geometric interpretations for the proposed safe MPC alignment process. Those properties will be used to establish the convergence of the algorithm.

1) *Piecewise Linear Cut:* By recalling the weight-feature parameterization of the safety constraint (5), one can examine that the inequities in (12) are both linear in θ . This means that the cutting set \mathcal{C}_i is a piecewise linear cut, as stated below.

Lemma 3. $\forall i$, \mathcal{C}_i in (12) can be expressed as an intersection of two half-spaces in \mathbb{R}^r :

$$\mathcal{C}_i = \{\theta \mid \theta^T \mathbf{h}_i \leq b_i\} \cap \{\theta \mid \theta^T \phi(\xi_{\theta_i}^\gamma) < -\phi_0(\xi_{\theta_i}^\gamma)\}, \quad (14)$$

with

$$\mathbf{h}_i = -\langle \bar{\mathbf{a}}_i, \nabla J(\xi_{\theta_i}^\gamma) \rangle \phi(\xi_{\theta_i}^\gamma) + \gamma \frac{\partial \phi}{\partial \mathbf{u}}(\xi_{\theta_i}^\gamma) \bar{\mathbf{a}}_i, \quad (15)$$

$$b_i = \langle \bar{\mathbf{a}}_i, \nabla J(\xi_{\theta_i}^\gamma) \rangle \phi_0(\xi_{\theta_i}^\gamma) - \gamma \langle \bar{\mathbf{a}}_i, \nabla \phi_0(\xi_{\theta_i}^\gamma) \rangle. \quad (16)$$

Proof. See Appendix A-B. \square

According to the above lemma, $\Theta_{i-1} \cap \mathcal{C}_i$ can be viewed as cutting Θ_{i-1} with two hyperplanes (Fig. 4):

$$\text{bd } \mathcal{C}_i = \{\theta \mid \theta^T \mathbf{h}_i = b_i, \theta^T \phi(\xi_{\theta_i}^\gamma) \leq -\phi_0(\xi_{\theta_i}^\gamma)\} \cup \{\theta \mid \theta^T \mathbf{h}_i \leq b_i, \theta^T \phi(\xi_{\theta_i}^\gamma) = -\phi_0(\xi_{\theta_i}^\gamma)\}, \quad (17)$$

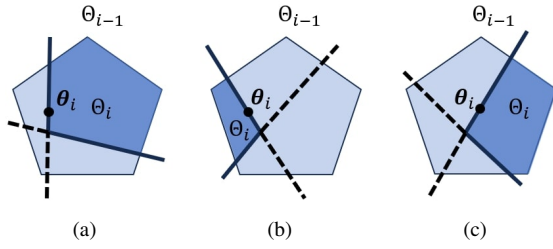


Fig. 5. Illustration of the different choices of θ_i . (a) and (b): When θ_i is chosen near the set boundary, the removed volume depends on the specific direction of cut $\text{bd } \mathcal{C}_i$. (c): When θ_i is near the center, the cut volume is large on average regardless of the specific user directional correction.

As the initial hypothesis space $\Theta_0 \subset \mathbb{R}^r$ in (10) is a convex polytope, iteratively cutting with hyperplanes yields a series of convex polytopes Θ_i s, $i = 0, 1, 2, \dots$

2) *Relationship between θ_i and $\text{bd } \mathcal{C}_i$:* The following assertion states a relationship between θ_i and $\text{bd } \mathcal{C}_i$.

Lemma 4. $\forall i$, θ_i is on $\text{bd } \mathcal{C}_i$ in (17). Specifically, θ_i satisfies

$$\theta_i^\top \mathbf{h}_i = b_i \quad \text{and} \quad \theta_i^\top \phi(\xi_{\theta_i}^\gamma) < -\phi_0(\xi_{\theta_i}^\gamma) \quad (18)$$

for all $i = 1, 2, \dots$

Proof. See Appendix A-C. \square

Lemma 4 states $\theta_i \in \text{bd } \mathcal{C}_i$. Its geometric interpretation is in Fig. 5(c): the cut $\text{bd } \mathcal{C}_i$ always passes θ_i . This suggests that the choice of $\theta_i \in \Theta_{i-1}$ is critical in the learning process: it directly affects the position of the cut $\text{bd } \mathcal{C}_i$ and consequently the removal volume. It is important to choose a good $\theta_i \in \Theta_{i-1}$ such that a large hypothesis space is removed after each cut.

We briefly discuss the implication of different choices of $\theta_i \in \Theta_{i-1}$. When choosing θ_i near the boundary of Θ_{i-1} , as in Fig. 5(b) and Fig. 5(a), the removal of the hypothesis space depends on the specific direction of cut $\text{bd } \mathcal{C}_i$. Since the direction of \mathcal{C}_i will be eventually determined by the direction of user correction according to (17), the removal of the hypothesis space can be relatively small, as in Fig. 5(b), or large, as in Fig. 5(a), depending on the specific direction of the correction.

As the specific direction of user correction is hard to assume, a good choice of $\theta_i \in \Theta_{i-1}$ will be near the center of Θ_{i-1} . As such, it can lead to an averaged large cut of the hypothesis space regardless of the direction of \mathcal{C}_i , as in Fig. 5(c). We will rigorously discuss the centering choice of θ_i and volume reduction rate of the hypothesis space in the next section.

V. IMPLEMENTATION DETAILS AND MAIN RESULTS

A. The Choice of θ_i

At each learning iteration i , based on the previous geometric intuition, our choice of θ_i is to achieve a large reduction of the hypothesis space for all possible human directional corrections. Thus, θ_i needs to be picked from the "center" of Θ_{i-1} . One option is to choose the mass center of Θ_{i-1} . However, computing the centroid of a polytope can be #P-Hard [51]. For computational efficiency, we choose θ_i as the center of the Maximum Volume Ellipsoid (MVE) inscribed in Θ_{i-1} ,

and will later compare its performance with other choices of θ_i in our experiments.

Definition 1 (Maximum Volume inscribed Ellipsoid (MVE) [52]). *The MVE of a given convex set $\Theta \subset \mathbb{R}^r$ is defined as the image of the unit ball under an affine transformation*

$$\mathcal{E} = \{\bar{H}\boldsymbol{\theta} + \bar{\mathbf{d}} \mid \|\boldsymbol{\theta}\|_2 \leq 1\}, \quad (19)$$

where the affine transformation parameter $\bar{H} \in \mathbb{S}_{++}^r$ (a $r \times r$ symmetric positive definite matrix), and $\bar{\mathbf{d}} \in \mathbb{R}^r$ is called the center of \mathcal{E} . $\bar{H}, \bar{\mathbf{d}}$ are determined via the following optimization problem to maximize the volume of the ellipsoid $\det H$:

$$\begin{aligned} \bar{H}, \bar{\mathbf{d}} = \arg \max_{H \in \mathbb{S}_{++}^r, \mathbf{d}} \quad & \log \det H \\ \text{s.t.} \quad & \sup_{\|\boldsymbol{\theta}\|_2 \leq 1} \mathbb{1}_\Theta(H\boldsymbol{\theta} + \mathbf{d}) \leq 0, \end{aligned} \quad (20)$$

where the indicator $\mathbb{1}_\Theta(\boldsymbol{\theta}) = 0$ for $\boldsymbol{\theta} \in \Theta$ and otherwise $\mathbb{1}_\Theta(\boldsymbol{\theta}) = +\infty$. Specifically, when Θ is a polytope $\{\boldsymbol{\theta}^\top \mathbf{n}_i \leq c_i, i = 1, \dots, m\}$, the problem can be converted to a convex optimization with m constraints, see chapter 8.4.2 in [52]:

$$\begin{aligned} \bar{H}, \bar{\mathbf{d}} = \arg \min_{H \in \mathbb{S}_{++}^r, \mathbf{d}} \quad & \log \det H^{-1} \\ \text{s.t.} \quad & \|H\mathbf{n}_i\|_2 + \mathbf{d}^\top \mathbf{n}_i \leq c_i, i = 1, \dots, m. \end{aligned} \quad (21)$$

Recall that in Safe MPC Alignment the learning update (13) is to iteratively cut the hypothesis space by hyperplanes (17), and that the initial hypothesis space (11) is a box. By induction, it leads to that any updated hypothesis space Θ_i is a convex polytope, $i = 0, 1, 2, \dots$. Thus, for any Θ_{i-1} , by the above definition, let \mathcal{E}_{i-1} denote the MVE of Θ_{i-1} and $\bar{\mathbf{d}}_{i-1}$ denote the center of \mathcal{E}_{i-1} . Then, the choice of θ_i is

$$\theta_i = \bar{\mathbf{d}}_{i-1}. \quad (22)$$

The convex optimization (20) can be solved efficiently [53].

B. Result 1: Finite Iteration Convergence

When choosing θ_i as the center of MVE of Θ_{i-1} , the following lemma states that the volume ratio $\text{Vol}(\Theta_i)/\text{Vol}(\Theta_{i-1})$ after each hypothesis space cut can be upper bounded.

Lemma 5. *In the Safe MPC Alignment, when choosing $\theta_i \in \mathbb{R}^r$ as the center of MVE of Θ_{i-1} , one has*

$$\frac{\text{Vol}(\Theta_i)}{\text{Vol}(\Theta_{i-1})} \leq 1 - \frac{1}{r}, \quad (23)$$

for all $i = 1, 2, 3, \dots$ and any enclosure volume measure Vol .

Proof. See Appendix A-D. \square

The lemma above asserts an upper bound of the volume of the hypothesis space $\text{Vol}(\Theta_i)$ relative to the previous volume. With this, we can now establish the finite iteration convergence of the *Safe MPC Alignment*, stated below.

Theorem 1 (Successful learning in finite iterations). *In the Safe MPC Alignment algorithm, θ_i is selected as the center of MVE of Θ_{i-1} , $i = 1, 2, 3, \dots$. If $\bar{\Theta}_H \subset \Theta_0$, the algorithm will terminate successfully within*

$$K = \left\lceil \frac{\ln \frac{\tau_r \rho_H^r}{\text{Vol}(\Theta_0)}}{\ln(1 - \frac{1}{r})} \right\rceil. \quad (24)$$

iterations, where ρ_H is the radius of a ball contained within $\bar{\Theta}_H$ and τ_r is the volume of a unit ball in \mathbb{R}^r space. That is, there exists $i < K$, such that $\theta_i \in \bar{\Theta}_H \subset \Theta_H$.

Proof. See Appendix A-E. \square

The above result asserts the maximum learning iteration to find $\theta_i \in \Theta_H$. In other words, within K rounds of human correction, the robot can successfully learn a safety constraint. The above result requires a pre-set of ρ_H^r , which is the radius of a ball contained in $\bar{\Theta}_H$. Since the size of $\bar{\Theta}_H$ is unknown in reality, $\rho_H > 0$ can be interpreted as an estimated size of the unknown user intent set $\bar{\Theta}_H$. It also serves as a termination threshold for learning convergence: a smaller ρ_H can lead to a more concentrated Θ_H at convergence.

The finite iteration convergence in Theorem 1 comes with a prerequisite: $\bar{\Theta}_H \in \Theta_0$ has to be satisfied in the first place for the Safe MPC Alignment. Although such a condition can be achieved by empirically choosing Θ_0 large enough to contain all possible $\bar{\Theta}_H$ (10), it is also desired to have a verification for the hypothesis misspecification, where such condition is not met. We will provide such result in the next subsection.

C. Result 2: Hypothesis Misspecification Certification

Consider hypothesis space misspecification, where $\bar{\Theta}_H \cap \Theta_0 = \emptyset$. In this case, no $\theta \in \Theta_0$ can account for the user intended safety (4). The hypothesis misspecification can lead to the undesired behavior of the robot [50], [54]. The following result states the Safe MPC Alignment can automatically certify the misspecification of Θ_0 .

Theorem 2 (Certifying misspecification). *In the Safe MPC Alignment, θ_i is selected as the center of MVE of Θ_{i-1} , $i = 1, 2, 3, \dots$. If $\bar{\Theta}_H \cap \Theta_0 = \emptyset$, the algorithm converges to a set Θ^* as $i \rightarrow \infty$, such that $\text{Vol}(\Theta^*) = 0$ and $\Theta^* \cap \text{int } \Theta_0 = \emptyset$.*

Proof. See Appendix A-F. \square

The above result states when the initial hypothesis space is misspecified, $\bar{\Theta}_H \cap \Theta_0 = \emptyset$, the Safe MPC Alignment algorithm will finally converge to a set of zero volume on the boundary of the initial hypothesis space Θ_0 . The above theorem inspires us to empirically identify the misspecification by monitoring the position of the MVE center of Θ_i during the learning update. As shown in Fig. 6, if after the maximum iteration $K - 1$ in (24), the MVE center θ_{K-1} is very close to the boundary of the initial hypothesis set Θ_0 , there is likely hypothesis space misspecification, and the algorithm terminates with misspecification failure.

Specifically, if Θ_0 is a box as defined in (10) with bounds c_l, c_h , we can pre-define a small threshold ϵ to examine if θ_{K-1} is on the boundary of Θ_0 . If θ_{K-1} satisfies

$$\min_{j=1, \dots, r} \min (|c_l[j] - \theta_{K-1}[j]|, |c_h[j] - \theta_{K-1}[j]|) \leq \epsilon \quad (25)$$

it means θ_{K-1} is very close to the boundary of Θ_0 . We consider there is likely misspecification in this case.

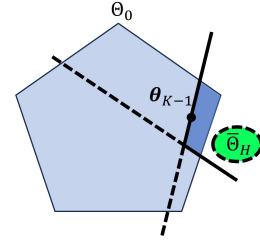


Fig. 6. When there is misspecification, the Safe MPC Alignment will converge to some point on the boundary of Θ_0 . So we can use the distance of θ_{K-1} to the boundary as an indicator for misspecification.

D. Detailed Algorithm of Safe MPC Alignment

With the main results on convergence and misspecification, we present the detailed algorithm in Algorithm 1. With Θ_0 and a termination threshold ρ_H pre-set, three steps in the hypothesis space cutting are executed until the user satisfies robot motion or the iteration count reaches the maximum count K in (24). Note that during the execution of the MPC policy $\pi_{\theta_i}^\gamma$, the human can perform emergency stopping and reset the robot's state, which corresponds to Section III-C3. After $K - 1$ iterations, the algorithm checks the misspecification by (25).

Algorithm 1: Safe MPC Alignment Algorithm

Initialization: Initial hypothesis space Θ_0 , termination threshold ρ_H , $i = 1$

Compute maximum iteration count K from ρ_H in (24);

while $i < K$ **do**

 Choose $\theta_i \in \Theta_{i-1}$ using (22);

 Robot executes $\pi_{\theta_i}^\gamma$;

if Human provides directional correction \mathbf{a}_{k_i} **then**

 Generate $\bar{\mathbf{a}}_i$ using (6);

 Calculate the cutting set \mathcal{C}_i using (14);

 Update hypothesis space $\Theta_i = \Theta_{i-1} \cap \mathcal{C}_i$;

$i \leftarrow i + 1$;

else if Human triggers emergency stop **then**

 Human restarts robot from safe region;

else if Human user is satisfied **then**

return θ_i ;

end

if θ_{K-1} satisfies (25) **then**

return misspecification failure;

else

return θ_{K-1}

end

VI. NUMERICAL EXAMPLES

In this section, we will evaluate the Safe MPC Alignment using two numerical examples: A pendulum task, where we will illustrate all theoretical aspects of the proposed method, and a thrust-controlled quadrotor navigation task, where we will demonstrate the capability of the method to learn safety constraints in complex 3D environments. Simulated human correction knowing ground-truth safety constraints will be used. We will compare the proposed method with baselines, and ablate the hyperparameters of the algorithm. All numerical experiments are implemented in Python, running on a desktop with Intel i9-13900K CPU. All our experiment codes are open-sourced at <https://github.com/asu-iris/Safe-MPC-Alignment>.

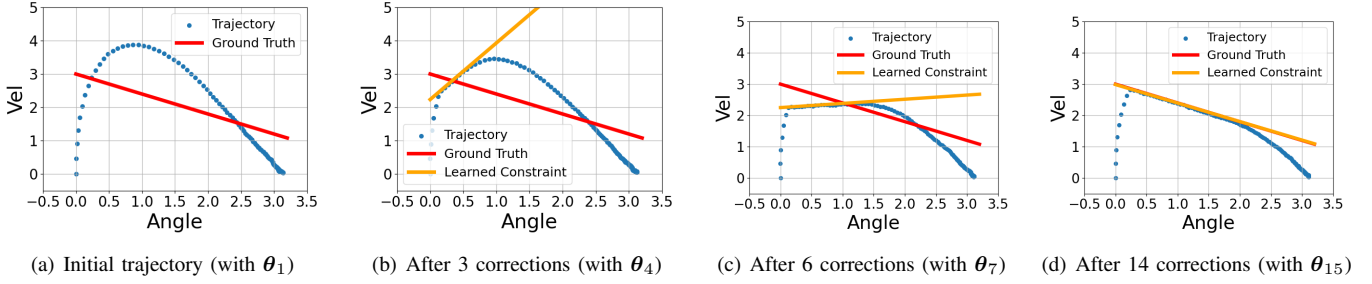


Fig. 7. The Safe MPC rollout trajectory after different learning interaction. The learned constraint with θ_1 is omitted since it covers the whole first quadrant. As learning proceeds, the constraint boundary (orange line) converges to the ground-truth (red line). When the learning process terminates, the learned and ground-truth constraint boundaries almost overlap, suggesting the success of constraint learning from correction.

A. Inverted Pendulum

1) *Setup*: The dynamics of an inverted pendulum is

$$\ddot{\alpha} = \frac{3}{ml^2} \left(-\frac{1}{2} mgl \sin \alpha + u - d\dot{\alpha} \right), \quad (26)$$

with α being the angle between the pendulum and gravity, g the gravity constant, u input torque, m , l and d the length, inertia, and damping ratio. The system state is $\mathbf{x} = [\alpha, \dot{\alpha}]^T$, (26) discretized by the Euler method with $\Delta t = 0.02s$. A zero-mean Gaussian noise with covariance $\Sigma = \mathbf{diag}(1, 4) \times 10^{-5}$ is added to \mathbf{x} at each MPC rollout to simulate the state noise. The task is to control the pendulum to a target $\mathbf{x}^* = [\pi, 0]^T$. We pose an unknown global state constraint on pendulum motion:

$$0.6\alpha + \dot{\alpha} = \boldsymbol{\theta}^H \mathbf{x} \leq 3, \quad (27)$$

where $\boldsymbol{\theta}^H = [0.6, 1]^T$ is to be learned. All other parameter values are given in Appendix.

In Safe MPC (1), we set $T = 40$ and the cost functions as

$$\begin{aligned} c(\mathbf{x}_t, u_t) &= Ru_t^2 \\ h(\mathbf{x}_T) &= (\mathbf{x}_T - \mathbf{x}^*)^T Q (\mathbf{x}_T - \mathbf{x}^*), \end{aligned} \quad (28)$$

respectively, with $R = 0.1$ and $Q = \text{diag}(25, 10)$. To ensure the safe MPC to satisfy a global constraint, it is sufficient to learn a safety constraint defined on the closest controllable state. Thus, we define

$$g_{\boldsymbol{\theta}}(\boldsymbol{\xi}) = -3 + \boldsymbol{\theta}^T \mathbf{x}_1. \quad (29)$$

In the penalty-based MPC (3), we set $\gamma = 0.1$.

Suppose the user intent set $\bar{\Theta}_H = \{\boldsymbol{\theta} \mid \|\boldsymbol{\theta} - \boldsymbol{\theta}_H\| \leq 0.02\}$. The simulated (synthetic) correction \mathbf{a} are generated as follows: when the system state is near the safety boundary, i.e., $g_{\boldsymbol{\theta}_H}(\boldsymbol{\xi}_{\boldsymbol{\theta}}^\gamma) > -\epsilon_g$ ($\epsilon_g = 0.25$ here), a directional correction \mathbf{a} is generated in probability $p = 0.3$ using $\text{sign}(-\nabla B(\boldsymbol{\xi}_{\boldsymbol{\theta}}^\gamma, \boldsymbol{\theta}_H))$ (from which only the first step is taken as in (6)). The correction is probabilistic to simulate the randomness of human providing corrections. It is easy to verify that the simulated \mathbf{a} is valid in term of satisfying the hypotheses in section IV-A.

2) *Convergence Analysis*: We first evaluate the convergence of our algorithm without hypothesis misspecification. In Algorithm 1, we set the initial hypothesis Θ_0 with box boundaries $\mathbf{c}_l = [-6, -6]^T$ and $\mathbf{c}_u = [2, 2]^T$; thus Θ_0 includes $\bar{\Theta}_H$. The initial $\boldsymbol{\theta}_1 = [-2, -2]^T$ (i.e., the center of Θ_0).

With each simulated correction, we track $\boldsymbol{\theta}_i$ in each learning update. Each update of Θ_i takes less than 30ms. $\boldsymbol{\theta}_i$ falls in

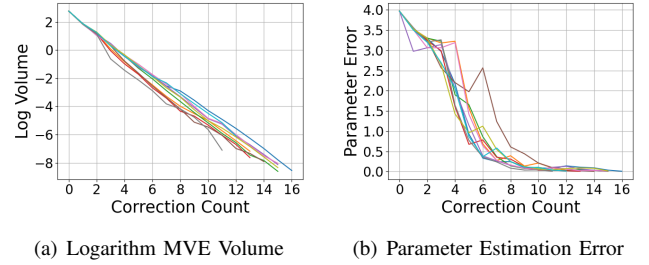


Fig. 8. (a) The plot of $\log \det \bar{H}$ with respect to correction numbers. In all algorithm runs (different colors), the plot shows the near-linear decrease of the logarithm volume, suggesting the exponential decrease of the volume of MVE of the hypothesis spaces, as asserted in Theorem 1. (b) The plot of the parameter estimation error $\|\boldsymbol{\theta}_i - \boldsymbol{\theta}_H\|_2$ versus correction numbers. In all runs, the parameter estimation error can converge to a value lower than 0.02 within 17 corrections, consistent with the theoretical bound in Theorem 1.

the ground-truth set $\bar{\Theta}_H$ after 14 corrections. The MPC rollout trajectory (phase plot) with each $\boldsymbol{\theta}_i$ is shown in Fig. 7. The ground-truth constraint (27) and the learned constraints $g_{\boldsymbol{\theta}_i}$ are also plotted. Fig. 7 shows that the true safety constraint can be successfully learned from simulated correction.

To analyze the convergence, we run the algorithm for 10 times. In each run, we keep track of two metrics over corrections (iterations) and show them in Fig. 8. The first metric (left panel) is the logarithm volume measure of the solved MVE $\log \det \bar{H}$ in (20); this provides a lower bound of the volume of Θ_i to show the exponential convergence. The second (right panel) is the parameter error $\|\boldsymbol{\theta}_i - \boldsymbol{\theta}_H\|_2$. From Fig. 8, we can conclude the proposed method is

- (I) Fast-converging. The logarithm volume $\log \det \bar{H}$ has a near-linear decreasing speed. This is consistent with the theory in Lemma 5.
- (II) Data-efficient. $\|\boldsymbol{\theta}_i - \boldsymbol{\theta}_H\|_2$ converges to the value lower than 0.02 within 17 corrections. This is consistent with the theoretical upper bound of correction count in Theorem 1:

$$\ln \frac{\tau_r \rho_H^r}{\text{Vol}(\Theta_0)} / \ln(1 - \frac{1}{r}) = 17.28. \quad (30)$$

3) *Misspecification Analysis*: To analyze the performance of our algorithm to certify misspecification cases, we set the initial hypothesis space Θ_0 as $\mathbf{c}_l = [-1, -1]^T$ and $\mathbf{c}_u = [0.8, 0.8]^T$ which does not contain $\bar{\Theta}_H$. In this setting, the algorithm automatically stops after 7th correction. The path of $\boldsymbol{\theta}_i$, $i =$

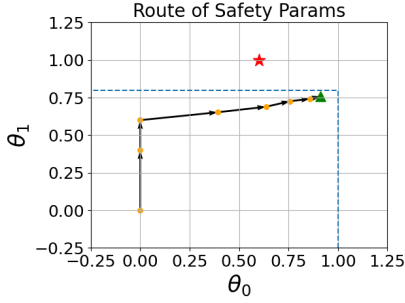


Fig. 9. Experiment of misspecification case. The blue dashed lines are the boundary of Θ_0 . Path of θ convergence, θ_i , $i = 1, \dots, 7$, is shown in orange dots with arrows showing the update direction. The ground-truth intent set is marked as the red star. Since misspecification happens for this case, θ will converge toward the boundary of Θ_0 (the green triangle). This is consistent with the statement in Theorem 2.

$1, \dots, 8$ is shown in Fig. 9. θ_i is continuously moving towards the boundary of Θ_0 . This fact verifies Theorem 2 and justifies the proposed method is capable of misspecification detection.

B. Quadrotor Navigation in Complex Environment

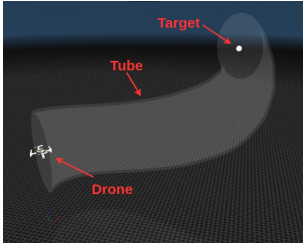


Fig. 10. Quadrotor navigation in an 3D zigzag tube.

1) *Setup*: We consider a thrust-controlled quadrotor navigating in an 3D zigzag tube, shown in Fig. 10. The simulation environment is based on MuJoCo [55], and the quadrotor dynamics follows [20]. Initially, the quadrotor has no knowledge of the safety constraint. When it nears the tube wall, a simulated (synthetic) correction is generated to push it away from the tube wall. Details of the setting are provided in Appendix B-B.

To learn positional safety constraints, we experiment with three feature vectors $\phi(\xi)$ in (5):

a) *Polynomial feature vector*: A vector of polynomial basis functions up to 3rd order to properly capture the zig-zag pattern of the tube) is defined in the quadrotors' 3D position $[x, y, z]$ at the 5th timestep in motion plan ξ :

$$\phi(\xi) = [x_5^3, y_5^3, z_5^3, x_5^2, y_5^2, z_5^2, x_5, y_5, z_5, x_5 y_5, y_5 z_5, x_5 z_5]^T. \quad (31)$$

The features are defined using the quadrotor's 3D position at the 5th prediction step. The hypothesis space is initialized as a box space with $c_l = [-80, \dots, -80]^T$ and $c_u = [200, \dots, 200]^T$. We select $\phi_0 = 1$ and $\gamma = 60$.

b) *Pre-trained neural feature vector*: We obtain the neural spacial features from a pre-trained Signed Distance Function (SDF) [56]. Specifically, we pre-train an SDF neural network using the point cloud data samples near the tube surface. This simulates the application where some geometric information of

the environment is available. The neural SDF is pre-trained in a regression-like manner, with distance, normal, and Eikonal losses (see details in Appendix B-B). With the pretrained SDF function, we take the 16-dimensional output of the second-to-last layer of the SDF network as our feature vector $\phi(\xi)$. The input to $\phi(\xi)$ is the quadrotor's 3D position $[x, y, z]$ at the 5th prediction step. Such a choice of feature vector $\phi(\xi)$ means that we will use the proposed Safe MPC Alignment to fine tune the last layer of the learned SDF, $g(\xi) = \theta^T \phi(\xi)$, for its safe navigation control.

To facilitate the real-time Safe MPC with the neural safety constraint $g(\xi) = \theta^T \phi(\xi)$, the optimization (1) uses the linearized $g(\xi)$ for calculation, which is linearized at the real robot state x_k^{real} . The initial bounds of the hypothesis space are set to $c_l = [-0.2, \dots, -0.2]^T$, $c_u = [0.1, \dots, 0.1]^T$. We select $\phi_0 = 0.1$ and $\gamma = 50$.

To ensure the feasibility of the learned constraint, in the above feature vectors, two additional cuts are added in each MVE update to enforce that the start and goal remain within the intended safe region. The task is successful if the drone reaches the goal without triggering this stop.

c) *Polynomial features with velocity features*: We consider the safety constraints are additionally defined in the velocity space. After learning the positional constraint with the polynomial feature vector, a new set of velocity-based features over all prediction steps, $\phi(\xi) = [\|v_1\|^2, \dots, \|v_{10}\|^2]^T$, is added. In this case, we will freeze the weights for polynomial features, and only learn the weights for velocity features. Our objective is to impose an additional constraint that caps the quadrotor's velocity magnitude below 0.45 [m/s], while ensuring that the previously learned positional constraint remains satisfied for collision avoidance. When the quadrotor's velocity exceeds a correction triggering threshold (0.4), a simulated correction is applied to push the quadrotor in the direction of negative velocity. The hypothesis space for the velocity features is initialized with bounds $c_l = [0, \dots, 0]^T$ and $c_u = [0.16, \dots, 0.16]^T$. We set the bias feature $\phi_0 = 1$ and select $\gamma = 100$.

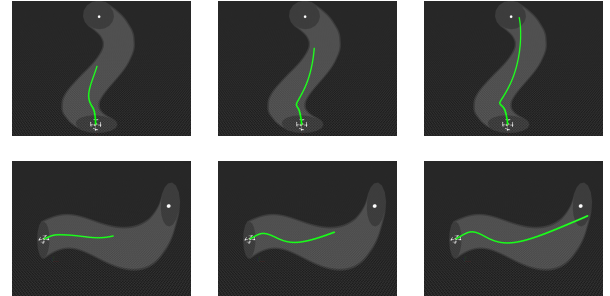


Fig. 11. The Safe MPC rollout trajectories (in green) for learning safety constraints with polynomial features after 26, 38, 45 corrections (different columns). The first row and second row show the top and the side views of the navigation environment.

2) *Result*: Fig. 11 and Fig. 12 show the rollout trajectories of the learned Safe MPC policy using polynomial and neural features, respectively. With polynomial features, the task is completed in 45 corrections, while the neural features require

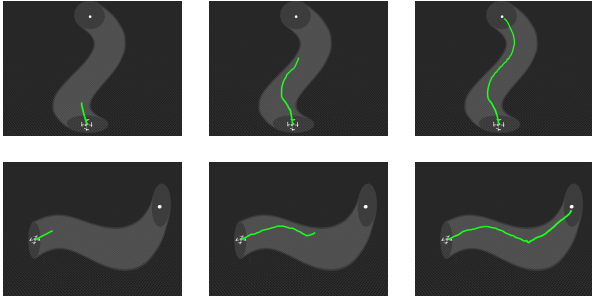


Fig. 12. The Safe MPC rollout trajectories (in green) for learning safety constraints with neural features after 6, 9, 11 corrections (different columns). The first row show the top view, and second row shows the side view of the navigation environment.

only 11. This is because the neural features, constructed from the second-to-last layer of pre-trained neural SDF, have already encoded the partial knowledge of spatial constraints.

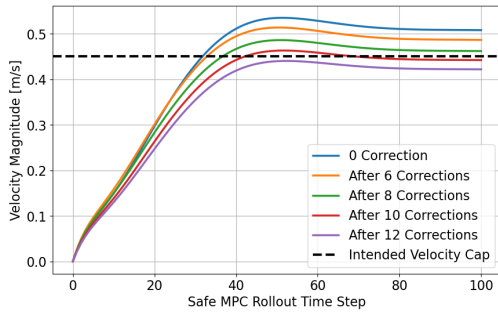


Fig. 13. Velocity profile during the first 100 timesteps (acceleration phase) of the drone trajectory. After 12 corrections, the quadrotor successfully learns to stay below the intended velocity cap of 0.45 (dashed line).

For the learning of velocity constraint, Fig. 13 shows the velocity profile of the quadrotor during the Safe MPC rollout in the 100 time steps (acceleration phase) after different number of simulated corrections (different colors). After 12 corrections, the quadrotor successfully learns to stay below the intended velocity cap of 0.45 (dashed line). Throughout this process, the positional safety constraint remains satisfied, with the quadrotor continuing to navigate within the tube to the target. This result demonstrates the flexibility of the proposed method in scenarios involving both positional and velocity constraints.

C. Baseline Comparison

In this session, we compare our method with two baseline methods using magnitude corrections in the pendulum environment. Since the literature on directly learning safety constraints from human feedback is sparse, the chosen baselines are an adaptation from the most relevant methods.

1) *Baseline 1: Gradient Matching*: This baseline is inspired by [57], where raw human correction (with magnitude) is directly used as the gradient direction. In a similar spirit, when a human correction \mathbf{a} is made on robot motion ξ_θ^γ , we directly use the human correction as the true gradient label to learn the constraint θ . This leads to a learning loss

$$\mathcal{L}(\theta) = \|\mathbf{a} + \nabla B(\xi_\theta^\gamma, \theta)\|^2. \quad (32)$$

2) *Baseline 2: Maximum Likelihood*: This baseline follows [58], where it views $e^{g_\theta(\xi)}$ as a probability of human applying the "stop-feedback" to robot motion ξ , when the robot reaches in a ϵ_g -proximity of the safety boundary, i.e., when $g_{\theta_H}(\xi_\theta^\gamma) > -\epsilon_g$. Thus, a dataset of trajectory-correction pairs, i.e., $\mathcal{D} = \{\mathbf{a}_i, \xi_i\}_{i=0}^N$, can be used as the training data to learn θ using maximum likelihood, while also penalizing positivity of $g_\theta(\xi_i)$ as a regularizer term. This leads to the following loss

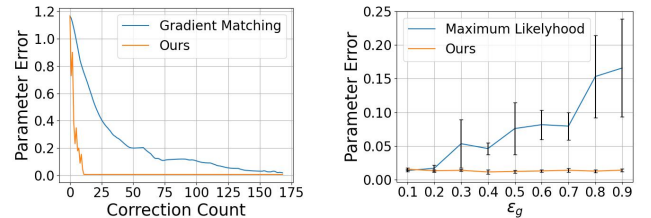
$$\mathcal{L}(\theta) = \sum_{i=1}^N (-g_\theta(\xi_i) + \alpha \cdot \text{softplus}(g_\theta(\xi_i))). \quad (33)$$

We choose $N = 15$ (similar to the correction number needed for our method to converge) and $\alpha = 5$ for its best performance.

The comparison between our method and the gradient matching baseline focuses on data efficiency. The convergence criteria of $\|\theta - \theta_H\| \leq 0.02$ is set for both methods. 50 independent runs are performed and the total number of correction at convergence are counted. We use Adam optimizer [59] with a learning rate of 0.02. We summarize the results in Table I. The parameter error $\|\theta - \theta_H\|$ versus learning iteration for a best run (for the baseline) is plotted in Fig. 14(a). The comparison results demonstrate data efficiency of the proposed method compared to the gradient matching baseline, even though the latter uses both magnitude and direction information of corrections to learn.

TABLE I
COMPARISON OF SAFE MPC ALIGNMENT AND BASELINE I

Method	Correction count for convergence
Safe MPC Alignment	11.76 ± 2.14
Gradient Matching	240.38 ± 120.70



(a) Comparison: gradient matching (b) Comparison: maximum likelihood

Fig. 14. (a) Comparison with gradient matching baseline: the parameter error $\|\theta - \theta_H\|$ versus learning iteration. This is best run with the fewest corrections for the baseline. Our method converges after 12 corrections, while the baseline needs more than 160 corrections. (b) Comparison with the maximum likelihood baseline under the different ϵ_g : the y-axis is $\|\theta - \theta_H\|$ at convergence with the error bar denoting the standard deviation. The maximum likelihood baseline fails to learn the correct weights when ϵ_g is large.

The comparison with maximum likelihood baseline uses the varying positions of simulated correction, i.e., varying ϵ_g . Recall that the simulated corrections are generated only when $g_{\theta_H}(\xi_\theta^\gamma) > -\epsilon_g$. The value of ϵ_g determines the position of correction. In our comparison, we vary ϵ_g from 0.1 to 0.9 and track the converged parameter error for both methods. As shown in Fig. 14(b), Safe MPC alignment consistently converges to the true θ_H regardless of ϵ_g , while the maximum likelihood baseline fails when $|\epsilon_g|$ is large. The results suggest the robustness of the proposed method against different correcting conditions compared to the maximum likelihood baseline.

D. Ablation Study

We conduct two ablation studies to show the performance of our algorithm given different design aspects. The task is still based on the pendulum task in Section VI-A.

1) Choosing θ_i : MVE centering versus random sampling:

We compare two strategies in selecting θ_i from the hypothesis space Θ_{i-1} : MVE centering (used in our method) and random sampling. For the latter, θ_i is sampled from the uniform distribution supported by Θ_{i-1} . We compare the total number of corrections at learning convergence under the two strategies.

With 50 independent runs, we observe the MVE centering requires 11.76 ± 2.14 corrections, while random sampling 11.88 ± 3.50 corrections. While the mean value of the correction count looks similar, the random sampling shows a slightly larger variance. This is understandable given sampling randomness. We also observed that the sampling process introduced a large computational overhead, which is around 25% time slower than MVE centering. In contrast, the MVE centering used in our algorithm shows low variance and computational efficiency. Because selecting θ_i is cast as a convex programming for MVE centering, such an advantage would be more significant for a high-dimensional parameter space.

2) Choosing γ : We study how the setting of γ affects the learning performance. We vary γ from 0.01 to 10. Fig. 15 shows the total number of corrections needed at convergence versus different γ s. The results show that the learning performance remains the same given different settings of γ . Since γ is a parameter to weigh the safety conservativeness in the penalty-based MPC (3), it means our method can successfully learn a safety constraint when the robot executes with a Safe MPC policy of different conservativeness levels.

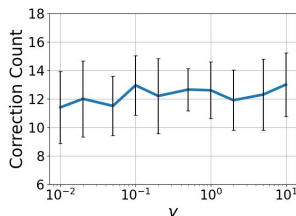


Fig. 15. The total number of corrections needed for convergence under different γ , the x-axis is of log scale.

VII. USER STUDY IN SIMULATION GAMES

We conduct two human user studies to evaluate the Safe MPC Alignment. One is the drone navigation game and the other the Franka robot arm reaching game. In both games, the robot is controlled by an MPC policy and human participants provide real-time corrections through a keyboard. The objective of each game is to teach a robot to successfully learn Safe MPC to move through environments with obstacles. Section VII-A describes the settings. Section VII-B details the user study procedure. The results are given in Section VII-C.

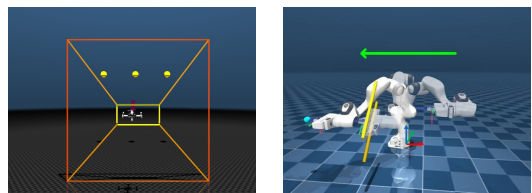
A. Two Simulation Games

In both user studies, human participants are asked to give correction to the following two physics-based simulation games developed based on MuJoCo [55].

(1) Drone Navigation Game. As shown in Fig. 16(a), the goal of this game is to let a drone to successfully navigate through a narrow gate (yellow rectangle), reaching different targets (shown in yellow points behind the gate). The safety constraint $\theta^T \phi$ is parameterized using a linear combination of spacial radial basis functions (RBFs), defined on y-z plane at $x = 10$. The drone’s control inputs are the thrusts of four rotors and human correction is applied via keyboard, with specific keys mapping to the drone’s control space. See the details in Appendix B-C.

(2) Franka arm reaching game. As shown in Fig. 16(b), the goal of the Franka arm reaching game is to teach a Franka arm such that its gripper hand successfully reaches different target positions (cyan ball) through an narrow slot (two yellow bars). Note that the safety constraint is only applied to the end effector and the collision between the link and the slot is ignored. The safety constraint function $\theta^T \phi$ is parameterized as a weighted combination of RBFs defined on the z axis and rotations around the x axis. Human corrections are applied via keyboard, with specific keys mapping to the robot control space \mathbb{R}^6 (we use operational space control). See the details in Appendix B-D.

In both games, the robots are controlled with Safe MPC policy (3) but fail to maintain safety with the initial safety constraints. To simulate an emergency stop, the “Enter” key is used as a reset command, allowing users to reset the environment to its initial state whenever the participant deems the robot violating the safety constraint.



(a) Drone Navigation game (b) Franka arm reaching game

Fig. 16. Two simulated games in user study. (a) Drone Navigation game. (b) Franka arm reaching game.

B. Participants, Procedures, and Metrics

1) *Participants*: We recruited 15 participants from Arizona State University, including undergraduates, masters, and PhD students with different backgrounds. Among all participants, 13 are male and 2 female. All participants are new to the user study. This user study had been reviewed and approved by the Institutional Review Board (IRB), and all participants had signed the consent forms.

2) *Procedure*: Each participant was asked to play the two simulation games. In each game, each participant plays 10 trials. In the drone navigation game, a trial is successful when the drone navigates through the gate without collision and reaches different targets 6 consecutive times with the learned safe MPC policy. A trial is deemed failed when there are too many corrections (exceeding 25), or the user believes the robot cannot be corrected anymore and gives up. In the Franka reaching game, a trial is deemed successful when the robot

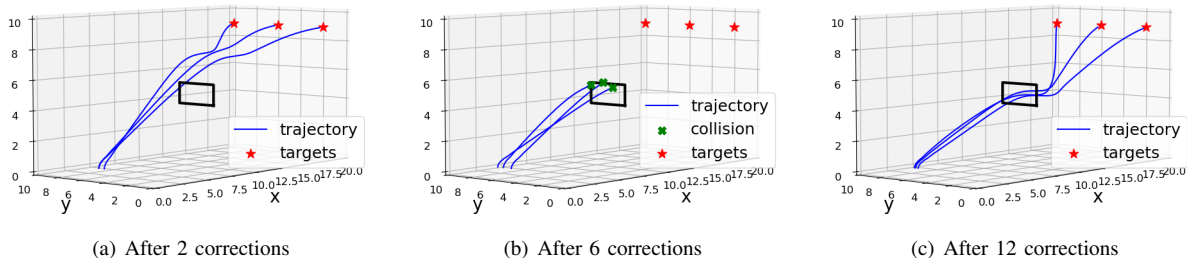


Fig. 17. Illustrations of the drone MPC rollout trajectory after 2, 6, 12 corrections. The red stars denote the targets and blue curves denote the trajectories. The gate is drawn as black frame and the collision is highlighted in green crosses. User corrections typically lower the drone to make it pass through the gate.

arm reaches different targets with the end-effector having no collision with the slot. The failure of one trial is determined when there are too many corrections (exceeding 25) or the user believes the robot cannot be corrected anymore and gives up. The result of every trial is recorded. Before formally starting the study, every user is instructed about the settings of the game and is given 2 chances to interact with the environment hands-on to get familiar with the keys.

3) *Metrics for Evaluation*: Two metrics are used to evaluate the outcomes: (I) *Success rate*: The overall success rate suggest the **effectiveness** of the proposed method. (II) *The number of corrections needed for a successful trial*: The averaged number of user corrections for successful trials is a measure for the **efficiency** of the proposed method. Fewer corrections in successful trials suggest better human data efficiency.

C. Result and Analysis

TABLE II
RESULT OF USER STUDY FOR SIMULATION GAMES

Environment	Success Rate	Correction count
Drone navigation	89.3% \pm 7.7%	15.7 \pm 10.6
Franka arm reaching	89.3% \pm 11.2%	16.5 \pm 6.1

1) *Results*: We report the success rate and correction count in a successful game trial in Table II. Both metrics are averaged across users. The success rate is 89.3% \pm 7.7% for the drone navigation game and 89.3% \pm 11.2% for the Franka arm reaching game. The number of corrections for a successful trial is 15.7 \pm 10.6 for the drone navigation game and 16.5 \pm 6.1 for Franka arm reaching game. In both games, each learning update of θ takes approximately 0.15 seconds, during which the simulation briefly pauses. This brief pause is imperceptible to the user, especially since human corrections occur infrequently.

The above result shows that the proposed method is effective (i.e., with a high success rate) in learning a safety constraint for varying tasks (recall targets are changing across trials). It also shows the efficiency of the proposed method: successful learning only requires tens of human corrections. Since this method is online and the user can perform multiple corrections in one robot rollout trajectory, the constraint can be learned in a few runs. In Table II, one can note that the drone navigation task has a higher variance in the correction count than the Franka arm reaching task. This could be because the drone

game has a larger motion range and longer rollout horizon. As a result, human correction strategies, such as correction position and timing, vary more.

2) *Analysis*: To illustrate learning progress, in Fig. 17 and Fig. 18, we show the intermediate robot motion after different numbers of human corrections. Fig. 17 shows the safe MPC rollout trajectory of the drone after different numbers of human corrections. Fig. 18 shows the keyframes of the robot gripper when passing the slot after a different human corrections.

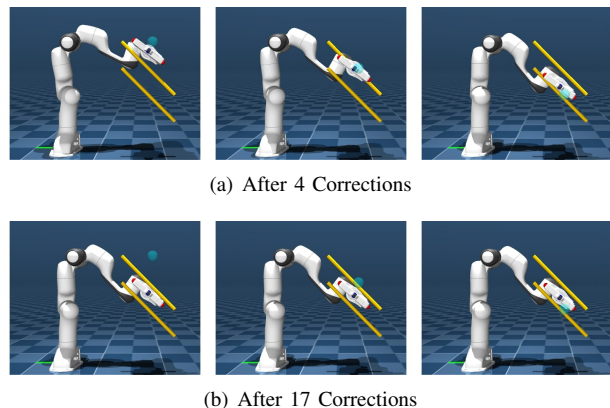


Fig. 18. Screenshots of the robot gripper when passing through the slot after $k = 4, 17$ corrections, given three different targets (cyan ball in different columns). (a): After 4 corrections, the gripper collides with the slot. (b): After 17 corrections, the gripper succeeds in passing the slot for all targets.

To understand the learned safety constraint $g_{\theta}(\xi)$, in Fig. 19, we draw the heat map of the learned $g_{\theta^*}(\xi)$ for the drone navigation game, with θ^* the averaged of weights learned. Recall in drone navigation game, g_{θ} is defined on y-z plane at $x = 10$. In the heat map, we draw 0-level contour of g_{θ^*} in dashed lines, which is the learned safety boundary. Also, we plot y-z plane projection of the gate, which is the black box.

Fig. 19 shows that the learned safety boundary (corresponding to $g_{\theta^*}(\xi) \leq 0$) is only similar to the top edge of the gate. This is explained below. As shown in Fig. 16(a), the targets are set higher than the gate, and thus during the learning process, the motion of the drone is always going up, as shown in Fig. 17. As a result, the majority of human corrections happen when the drone approaches the top edge of the gate, leaving the learned safety boundary accurate near the top edge of the gate and bottom edge untouched. It is expected that to learn a safety constraint that fully represents the gate, lower target

positions should be added so that the drone will receive human corrections near the bottom edge of the gate.

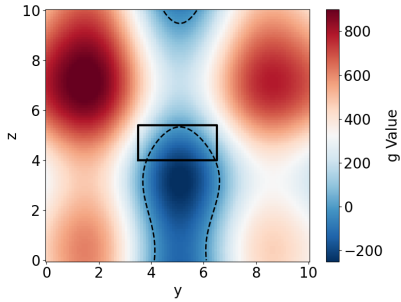


Fig. 19. Heatmap for the learned constraint in the drone game. The black solid line denotes the actual position of the gate in y - z plane. The black dashed curve denotes the boundary of the learned safety zone. Since the majority of human directional corrections happen when the drone approaches the top edge of the gate, the learned safety boundary is accurate near the top edge of the gate and the bottom boundary is untouched.

VIII. REAL-WORLD EXPERIMENT

We conduct a user study to evaluate the performance of the Safe MPC Alignment in a real-world experiment. We focus on the task of *mobile liquid pouring*: the Franka robot arm performs liquid pouring while moving from one location to targets. The task is challenging because it is hard to manually define a safety constraint to accomplish liquid pouring without spilling. The robot arm will learn a safe MPC controller from human physical corrections.

A. Hardware Setup

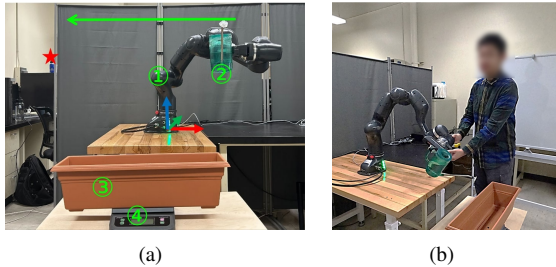


Fig. 20. Illustration images of the real-world experiment. (a) Mobile water pouring task using Franka robot arm. ①: The robot arm. ②: The watering pot. ③: The bar sink. ④: The scale to measure the amount of water poured into the sink. The target is marked as the red star. The long arrow indicates the motion direction, and the RGB frame is the world frame. (b) Illustration of human correction to the robot in the real-world experiment, by applying a contact force to the robot arm. The delta position of the end effector resulting from human contact interaction is used as human directional correction.

The setup of the mobile water pouring task is shown in Fig. 20(a). A water pot is gripped by the robot’s end-effector. The robot moves from the starting point $[0.22, -0.5, 0.48]^T$ (with quaternion $[0, -0.707, 0, 0.707]^T$) to target point $[-0.65, -0.5, 0.5]^T$ (with quaternion $[0, -0.707, 0, 0.707]^T$). During the motion, the robot needs to pour more than 50 grams of water into a bar sink. The bar sink is placed in the middle of the robot’s path, but the precise size and location of the bar sink are unknown.

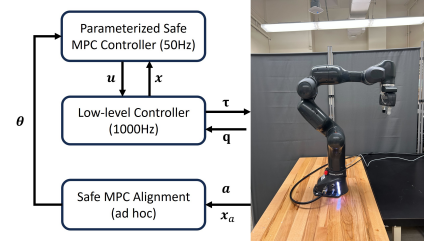


Fig. 21. System diagram for the hardware implementation. Different blocks indicate separate processes communicated via ROS.

Fig. 21 shows three main components of the system: the parameterized Safe MPC controller (high-level controller), the low-level controller, and the Safe MPC alignment module. The Safe MPC controller follows the safe MPC formulation of Franka arm reaching game in Appendix B-D (recall that the learnable safety constraint is parameterized by RBFs). The parameters of this Safe MPC controller are listed in Table III. The Safe MPC controller receives the end-effector’s current pose x and generates the action u (see (59) in Appendix), which is the desired velocity of the end-effector. The low-level controller implements the operational space control to track the u given by the safe MPC controller.

The Safe MPC Alignment module updates the parameter θ of the Safe MPC controller. The update only happens when the alignment module detects a human correction a . The module implements our Safe MPC Alignment algorithm. Note that the alignment module and controller modules runs in different processes, thus the learning update does not affect the real-time MPC control of the robot arm. ROS is used for communication between different processes.

TABLE III
PARAMETER LIST IN REAL-WORLD USER STUDY

Parameter	Value
Q_r	$\text{diag}(0.8, 0.8, 0.8)$
k_q	0
R_v	$\text{diag}(30, 30, 1)$
R_w	$\text{diag}(0.85, 0.85, 0.85)$
S_r	$\text{diag}(80, 80, 80)$
μ_q	80

As shown in Fig. 20(b), to give a physical correction to the Franka robot arm, a human user need physically touch/hold any link of the robot arm, and the applied force will immediately activate the zero-torque control mode. Suppose the joint positions of the robot arm before and after human physical correction are $\mathbf{q}_{\text{before}}$ and $\mathbf{q}_{\text{after}}$, respectively, we calculate the corresponding raw human correction \mathbf{a}_r using

$$\mathbf{a}_r = \mathbf{J}(\mathbf{q}_{\text{before}})(\mathbf{q}_{\text{after}} - \mathbf{q}_{\text{before}}), \quad (34)$$

with \mathbf{J} the Jacobian of the end-effector. The calculated $\mathbf{a}_r \in \mathbb{R}^6$ is considered as the displacement of the end-effector pose, intended by the human user.

B. Participants, Procedures, and Metrics

All participants recruited in Section VII-B also participate in the hardware experiment. They are told of the objective before

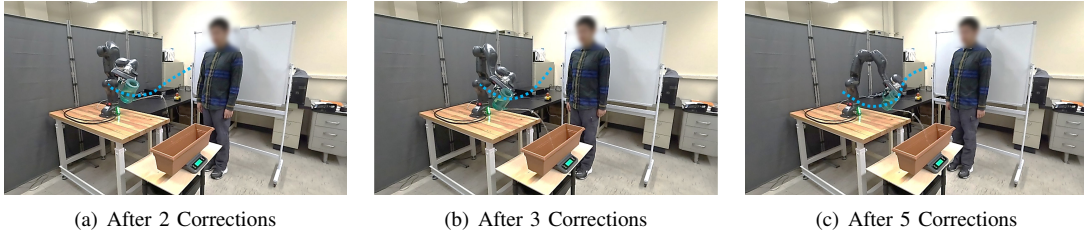


Fig. 22. Illustrations of one trial of the real-world experiment. The trajectories of the watering pot is denoted by blue dashed lines. (a) After 2 corrections, the arm begins tilting the pot but spills out the water. (b) After 3 corrections, the arm can pour water into the sink but the human is not satisfied with its height and the altitude of pouring. (c) After 5 corrections, the arm learns to tilt only along the direction of the x -axis and successfully aligns with human intent.

starting trials. One episode is defined as one robot motion from the starting position to the targets, during which the human can apply corrections at any time instances. One learning trial may include multiple episodes (with a maximum of 15 corrections). During learning, the nozzle of the water pot is sealed, and we switch to the unsealed nozzle and measure the amount of water poured into the flower pot after the user is satisfied with the motion of the robot. The successful trial is defined when the amount of poured water is over 50g. Each user performs 5 trials, and the same metrics in Section VII-B are recorded.

C. Result and Analysis

In the real-world experiment, the success rate is $84.0\% \pm 16.7\%$ and the average number of corrections needed for successful trials is 6.88 ± 3.26 . The results show the efficacy and efficiency of our method in real-world applications. To illustrate the learning progress, Fig. 22 shows the robot behavior after different numbers of corrections in one trial.

Since this real-world Franka arm experiment is similar to the simulated Franka arm reaching game in Appendix B-D, we compare the user study results for both and have the following conclusion and analysis.

(I) *Real-world experiment has slightly lower success rate:* While the difference between simulation and real-world studies is small in success rate, we have identified some factors for such a difference. On human aspects, most of the participants have no experience or knowledge in operating robot hardware, and thus when directly interacting with hardware, their corrections can be conservative or ineffective due to safety considerations. On hardware side, noisy correction signals and the possible timing delay between the recorded correction and the robot state can contribute to failure.

(II) *Real-world experiment needs less human corrections:* This could be attributed to two reasons. First, the constraint needed for accomplishing the water pouring task could be more flexible than that for reaching task in the simulation game. This makes the safety constraints easy to learn for the real-world task. Second, different from simulation games, where human users can only perceive the robot arm from the screen, a human user has a better perception of the robot's motion in the real world. A good perception of the robot's state could help humans give more effective feedback each time, reducing the total number of human interactions for successful robot learning.

IX. DISCUSSION AND CONCLUSION

A. Discussion

Based on the above hardware and simulation user studies, we discuss some design choices and potential limitations of the proposed method.

1) *Learning Task-Independent Safety Constraints:* In the real-world and simulation experiments, the learned safety constraint could be task-specific, instead of task-independent. For instance, in the drone navigation game, since the three task targets are placed above the gate, the learned constraint shown in Fig. 19 can only reflect the upper edge of the unknown gate. One limitation is that the learned constraints have poor generalization to new tasks. For example, in drone navigation, if a new target is placed below the gate, the drone with the learned safety constraint Fig. 19 will fail.

To improve the generalization of the learned safety constraints or learning task-independent safety constraints, one solution is to increase the diversity of task samples. By doing so, it is expected that the robot can receive human correction on the entire boundary of the safety region.

2) *Robustness Against Human Mistakes:* The proposed Safe MPC Alignment is based on the hypothesis cutting. In our formulation, a hypothesis cut (7) is based on an average of multiple human corrections, such an averaging treatment can mitigate human mistakes for one cut. But still, in practice, human irrationality can lead to the wrong cut of the hypothesis space, which is the main reason for failure in user studies. For example, in the drone navigation game, we found that failure game trials usually happen when a human gives too many wrong directional corrections. A failure case is in Fig. 23.

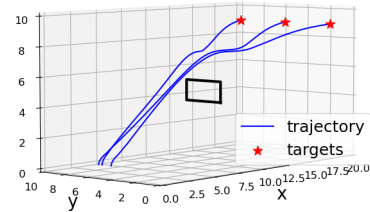


Fig. 23. A failure case in the drone game user study. A user makes a wrong "up" correction at the beginning and fails to correct the motion of the drone.

To further improve the robustness of the method against human mistakes, two extensions of the current method can be

explored. The first is to add a relaxation factor $\epsilon \geq 0$ in our cutting hypothesis. For example, we can re-write (7) as

$$\forall \theta_H \in \bar{\Theta}_H, \mathbb{E}_{\mathbf{a}} \langle \mathbf{a}, -\nabla B(\xi_{\theta}^{\gamma}, \theta_H) \rangle + \epsilon \geq 0. \quad (35)$$

Another is to add a selection mechanism for human correction. For example, one can use a voting system to preserve more fraction of the hypothesis space and avoid cutting out the human safety set, as shown in [60].

3) *Limitation of Weight-Feature Constraints*: In this work, we assume the set of task-relevant features in $\phi(\xi)$ is selected as a priori. These features define the space in which the safety constraints are represented. However, in practice, identifying appropriate features can be challenging. Poorly chosen features may fail to capture the intended safety constraints, leading to undesired learning outcomes. Furthermore, feature representations are often task-dependent—features that are effective in one task may not generalize to another. This task-specific dependence inherently limits the development of a unified framework for constraint learning across diverse tasks, making the lack of task-generalizable feature selection a key limitation of the proposed method. At the same time, learning unstructured constraints entirely from scratch would demand extensive human interaction and involvement, rendering such approaches impractical for most real-world applications. This challenge likely explains why recent works on learning from human feedback [13], [18], [20] commonly assume task-specific feature structures or prior knowledge of the environment/tasks.

We recognize that identifying or learning a universal feature representation that can flexibly describe a wide variety of safety constraints remains an important and open research challenge. We consider this an exciting direction for future research, as it could significantly increase the applicability and effectiveness of safety constraint learning in real world.

B. Conclusion

This paper proposes a Safe MPC Alignment method to online learn a safety constraint in Safe MPC controllers from human directional feedback. The method, named hypothesis space cutting, has a geometric interpretation: it exponentially cuts the hypothesis space based on each received human directional feedback. To our knowledge, this is the first certifiable method to enable online learning of safety constraints with human feedback. The method has a provable guarantee for the total number of human feedback needed for learning, and also can declare hypothesis misspecification. Numeric examples, user studies on simulation games, and a user study on the real-world robot arm, covering varying robot tasks, were used to validate the effectiveness of the proposed approach. The results show that the proposed method can learn safety constraints effectively and efficiently.

REFERENCES

- [1] Kim P Wabersich, Andrew J Taylor, Jason J Choi, Koushil Sreenath, Claire J Tomlin, Aaron D Ames, and Melanie N Zeilinger. Data-driven safety filters: Hamilton-jacobi reachability, control barrier functions, and predictive methods for uncertain systems. *IEEE Control Systems Magazine*, 43(5):137–177, 2023.
- [2] Shangding Gu, Long Yang, Yali Du, Guang Chen, Florian Walter, Jun Wang, Yaodong Yang, and Alois Knoll. A review of safe reinforcement learning: Methods, theory and applications. *arXiv preprint arXiv:2205.10330*, 2022.
- [3] Glen Chou, Dmitry Berenson, and Necmiye Ozay. Learning constraints from demonstrations. In *Algorithmic Foundations of Robotics XIII: Proceedings of the 13th Workshop on the Algorithmic Foundations of Robotics 13*, pages 228–245. Springer, 2020.
- [4] David Lindner, Xin Chen, Sebastian Tschitschek, Katja Hofmann, and Andreas Krause. Learning safety constraints from demonstrations with unknown rewards. *arXiv preprint arXiv:2305.16147*, 2023.
- [5] Dexter RR Scobee and S Shankar Sastry. Maximum likelihood constraint inference for inverse reinforcement learning. *arXiv preprint arXiv:1909.05477*, 2019.
- [6] Paul F Christiano, Jan Leike, Tom Brown, Miljan Martic, Shane Legg, and Dario Amodei. Deep reinforcement learning from human preferences. *Advances in neural information processing systems*, 30, 2017.
- [7] Dorsa Sadigh, Anca D Dragan, S. Shankar Sastry, and Sanjit A. Seshia. Active preference-based learning of reward functions. In *Robotics: Science and Systems*, 2017.
- [8] Borja Ibarz, Jan Leike, Tobias Pohlen, Geoffrey Irving, Shane Legg, and Dario Amodei. Reward learning from human preferences and demonstrations in atari. *Advances in neural information processing systems*, 31, 2018.
- [9] Kimin Lee, Laura M Smith, and Pieter Abbeel. Pebble: Feedback-efficient interactive reinforcement learning via relabeling experience and unsupervised pre-training. In Marina Meila and Tong Zhang, editors, *Proceedings of the 38th International Conference on Machine Learning*, volume 139 of *Proceedings of Machine Learning Research*, pages 6152–6163. PMLR, 18–24 Jul 2021.
- [10] Donald Joseph Hejna III and Dorsa Sadigh. Few-shot preference learning for human-in-the-loop rl. In *Conference on Robot Learning*, pages 2014–2025. PMLR, 2023.
- [11] Vivek Myers, Erdem Biyik, and Dorsa Sadigh. Active reward learning from online preferences. In *2023 IEEE International Conference on Robotics and Automation (ICRA)*, pages 7511–7518, 2023.
- [12] Vivek Myers, Erdem Biyik, Nima Anari, and Dorsa Sadigh. Learning multimodal rewards from rankings. In Aleksandra Faust, David Hsu, and Gerhard Neumann, editors, *Proceedings of the 5th Conference on Robot Learning*, volume 164 of *Proceedings of Machine Learning Research*, pages 342–352. PMLR, 08–11 Nov 2022.
- [13] Andrea Bajcsy, Dylan P Losey, Marcia K O’Malley, and Anca D Dragan. Learning robot objectives from physical human interaction. In *Conference on robot learning*, pages 217–226. PMLR, 2017.
- [14] Dylan P Losey and Marcia K O’Malley. Including uncertainty when learning from human corrections. In *Conference on Robot Learning*, pages 123–132. PMLR, 2018.
- [15] Andrea Bajcsy, Dylan P Losey, Marcia K O’Malley, and Anca D Dragan. Learning from physical human corrections, one feature at a time. In *Proceedings of the 2018 ACM/IEEE International Conference on Human-Robot Interaction*, pages 141–149, 2018.
- [16] Jason Y Zhang and Anca D Dragan. Learning from extrapolated corrections. In *2019 International Conference on Robotics and Automation (ICRA)*, pages 7034–7040. IEEE, 2019.
- [17] Mengxi Li, Alper Canberk, Dylan P Losey, and Dorsa Sadigh. Learning human objectives from sequences of physical corrections. In *2021 IEEE International Conference on Robotics and Automation (ICRA)*, pages 2877–2883. IEEE, 2021.
- [18] Dylan P Losey, Andrea Bajcsy, Marcia K O’Malley, and Anca D Dragan. Physical interaction as communication: Learning robot objectives online from human corrections. *The International Journal of Robotics Research*, 41(1):20–44, 2022.
- [19] Shaunak A Mehta and Dylan P Losey. Unified learning from demonstrations, corrections, and preferences during physical human-robot interaction. *ACM Transactions on Human-Robot Interaction*, 2023.
- [20] Wanxin Jin, Todd D Murphey, Zehui Lu, and Shaoshuai Mou. Learning from human directional corrections. *IEEE Transactions on Robotics*, 39(1):625–644, 2022.
- [21] Andrew Y Ng, Stuart Russell, et al. Algorithms for inverse reinforcement learning. In *Icml*, volume 1, page 2, 2000.
- [22] Pieter Abbeel and Andrew Y Ng. Apprenticeship learning via inverse reinforcement learning. In *Proceedings of the twenty-first international conference on Machine learning*, page 1, 2004.
- [23] Nathan D Ratliff, J Andrew Bagnell, and Martin A Zinkevich. Maximum margin planning. In *Proceedings of the 23rd international conference on Machine learning*, pages 729–736, 2006.

- [24] Brian D Ziebart, Andrew L Maas, J Andrew Bagnell, Anind K Dey, et al. Maximum entropy inverse reinforcement learning. In *Aaai*, volume 8, pages 1433–1438. Chicago, IL, USA, 2008.
- [25] Katja Mombaur, Anh Truong, and Jean-Paul Laumond. From human to humanoid locomotion—an inverse optimal control approach. *Autonomous robots*, 28:369–383, 2010.
- [26] Peter Englert, Ngo Anh Vien, and Marc Toussaint. Inverse kkt: Learning cost functions of manipulation tasks from demonstrations. *The International Journal of Robotics Research*, 36(13-14):1474–1488, 2017.
- [27] Harish Ravichandar, Athanasios S Polydoros, Sonia Chernova, and Aude Billard. Recent advances in robot learning from demonstration. *Annual review of control, robotics, and autonomous systems*, 3:297–330, 2020.
- [28] Ashesh Jain, Shikhar Sharma, Thorsten Joachims, and Ashutosh Saxena. Learning preferences for manipulation tasks from online coactive feedback. *The International Journal of Robotics Research*, 34(10):1296–1313, 2015.
- [29] Ralph Allan Bradley and Milton E Terry. Rank analysis of incomplete block designs: I. the method of paired comparisons. *Biometrika*, 39(3/4):324–345, 1952.
- [30] Siddharth Karamcheti, Raj Palleli, Yuchen Cui, Percy Liang, and Dorsa Sadigh. Shared autonomy for robotic manipulation with language corrections. In *ACL Workshop on Learning with Natural Language Supervision*, 2022.
- [31] Yuchen Cui, Siddharth Karamcheti, Raj Palleli, Nidhya Shivakumar, Percy Liang, and Dorsa Sadigh. No, to the right: Online language corrections for robotic manipulation via shared autonomy. In *Proceedings of the 2023 ACM/IEEE International Conference on Human-Robot Interaction*, pages 93–101, 2023.
- [32] Megha Srivastava, Noah Goodman, and Dorsa Sadigh. Generating language corrections for teaching physical control tasks. In *International Conference on Machine Learning*, pages 32561–32574. PMLR, 2023.
- [33] Lihan Zha, Yuchen Cui, Li-Heng Lin, Minae Kwon, Montserrat G. Arenas, Andy Zeng, Fei Xia, and Dorsa Sadigh. Distilling and retrieving generalizable knowledge for robot manipulation via language corrections. In *International Conference on Robotics and Automation (ICRA)*, may 2024.
- [34] Lucy Xiaoyang Shi, Zheyuan Hu, Tony Z Zhao, Archit Sharma, Karl Pertsch, Jianlan Luo, Sergey Levine, and Chelsea Finn. Yell at your robot: Improving on-the-fly from language corrections. *arXiv preprint arXiv:2403.12910*, 2024.
- [35] Glen Chou, Necmiye Ozay, and Dmitry Berenson. Learning parametric constraints in high dimensions from demonstrations. In *Conference on Robot Learning*, pages 1211–1230. PMLR, 2020.
- [36] Ashish Gaurav, Kasra Rezaee, Guiliang Liu, and Pascal Poupart. Learning soft constraints from constrained expert demonstrations. In *The Eleventh International Conference on Learning Representations*, 2023.
- [37] Konwoo Kim, Gokul Swamy, Zuxin Liu, Ding Zhao, Sanjiban Choudhury, and Steven Z Wu. Learning shared safety constraints from multi-task demonstrations. *Advances in Neural Information Processing Systems*, 36, 2024.
- [38] Glen Chou, Necmiye Ozay, and Dmitry Berenson. Learning constraints from locally-optimal demonstrations under cost function uncertainty. *IEEE Robotics and Automation Letters*, 5(2):3682–3690, 2020.
- [39] Glen Chou, Dmitry Berenson, and Necmiye Ozay. Uncertainty-aware constraint learning for adaptive safe motion planning from demonstrations. In *Conference on Robot Learning*, pages 1612–1639. PMLR, 2021.
- [40] Glen Chou, Hao Wang, and Dmitry Berenson. Gaussian process constraint learning for scalable chance-constrained motion planning from demonstrations. *IEEE Robotics and Automation Letters*, 7(2):3827–3834, 2022.
- [41] Kaylene C Stocking, D Livingston McPherson, Robert P Matthew, and Claire J Tomlin. Maximum likelihood constraint inference on continuous state spaces. In *2022 International Conference on Robotics and Automation (ICRA)*, pages 8598–8604. IEEE, 2022.
- [42] Shehryar Malik, Usman Anwar, Alireza Aghasi, and Ali Ahmed. Inverse constrained reinforcement learning. In *International conference on machine learning*, pages 7390–7399. PMLR, 2021.
- [43] David L McPherson, Kaylene C Stocking, and S Shankar Sastry. Maximum likelihood constraint inference from stochastic demonstrations. In *2021 IEEE Conference on Control Technology and Applications (CCTA)*, pages 1208–1213. IEEE, 2021.
- [44] Mattijs Baert, Pietro Mazzaglia, Sam Leroux, and Pieter Simoons. Maximum causal entropy inverse constrained reinforcement learning. *arXiv preprint arXiv:2305.02857*, 2023.
- [45] Daehyung Park, Michael Noseworthy, Rohan Paul, Subhro Roy, and Nicholas Roy. Inferring task goals and constraints using bayesian nonparametric inverse reinforcement learning. In *Conference on robot learning*, pages 1005–1014. PMLR, 2020.
- [46] Dimitris Papadimitriou, Usman Anwar, and Daniel S Brown. Bayesian methods for constraint inference in reinforcement learning. *Transactions on Machine Learning Research*, 2022.
- [47] Wanxin Jin, Shaoshuai Mou, and George J Pappas. Safe pontryagin differentiable programming. *Advances in Neural Information Processing Systems*, 34:16034–16050, 2021.
- [48] Ruohan Zhang, Dhruva Bansal, Yilun Hao, Ayano Hiranaka, Jialu Gao, Chen Wang, Roberto Martín-Martín, Li Fei-Fei, and Jiajun Wu. A dual representation framework for robot learning with human guidance. In *Conference on Robot Learning*, pages 738–750. PMLR, 2023.
- [49] Erdem Bıyık, Aditi Talati, and Dorsa Sadigh. Aprel: A library for active preference-based reward learning algorithms. In *2022 17th ACM/IEEE International Conference on Human-Robot Interaction (HRI)*, pages 613–617. IEEE, 2022.
- [50] Andreea Bobu, Andrea Bajcsy, Jaime F Fisac, Sampada Deglurkar, and Anca D Dragan. Quantifying hypothesis space misspecification in learning from human–robot demonstrations and physical corrections. *IEEE Transactions on Robotics*, 36(3):835–854, 2020.
- [51] Luis A Rademacher. Approximating the centroid is hard. In *Proceedings of the twenty-third annual symposium on Computational geometry*, pages 302–305, 2007.
- [52] Stephen P Boyd and Lieven Vandenberghe. *Convex optimization*. Cambridge university press, 2004.
- [53] Inc. CVX Research. CVX: Matlab software for disciplined convex programming, version 2.0. <http://cvxr.com/cvx>, August 2012.
- [54] Gaurav R Ghosal, Matthew Zurek, Daniel S Brown, and Anca D Dragan. The effect of modeling human rationality level on learning rewards from multiple feedback types. In *Proceedings of the AAAI Conference on Artificial Intelligence*, volume 37, pages 5983–5992, 2023.
- [55] Emanuel Todorov, Tom Erez, and Yuval Tassa. Mujoco: A physics engine for model-based control. In *2012 IEEE/RSJ International Conference on Intelligent Robots and Systems*, pages 5026–5033. IEEE, 2012.
- [56] Jeong Joon Park, Peter Florence, Julian Straub, Richard Newcombe, and Steven Lovegrove. DeepSDF: Learning continuous signed distance functions for shape representation. In *Proceedings of the IEEE/CVF conference on computer vision and pattern recognition*, pages 165–174, 2019.
- [57] Dylan P Losey and Marcia K O’Malley. Learning the correct robot trajectory in real-time from physical human interactions. *ACM Transactions on Human-Robot Interaction (THRI)*, 9(1):1–19, 2019.
- [58] Silvia Poletti, Alberto Testolin, and Sebastian Tschiatschek. Learning constraints from human stop-feedback in reinforcement learning. In *Proceedings of the 2023 International Conference on Autonomous Agents and Multiagent Systems*, pages 2328–2330, 2023.
- [59] P Kingma Diederik. Adam: A method for stochastic optimization. (*No Title*), 2014.
- [60] Zhixian Xie, Haode Zhang, Yizhe Feng, and Wanxin Jin. Robust reward alignment via hypothesis space batch cutting. *arXiv preprint arXiv:2502.02921*, 2025.
- [61] Sergei Pavlovich Tarasov. The method of inscribed ellipsoids. In *Soviet Mathematics-Doklady*, volume 37, pages 226–230, 1988.
- [62] Joseph Ortiz, Alexander Clegg, Jing Dong, Edgar Sucar, David Novotny, Michael Zollhoefer, and Mustafa Mukadam. isdf: Real-time neural signed distance fields for robot perception. *arXiv preprint arXiv:2204.02296*, 2022.

APPENDIX A

PROOF OF LEMMAS AND THEOREMS

A. Proof of Lemma 2

Proof. We prove this lemma by induction. First, we have $\bar{\Theta}_H \subset \Theta_0$. Suppose $\bar{\Theta}_H \subset \Theta_{i-1}$, $i = 1, 2, 3, \dots$. From the previous assumptions (7) and (9), $\bar{\Theta}_H \subset \mathcal{C}_i$. Following the update (13), we have $\bar{\Theta}_H \subset \Theta_i = \Theta_{i-1} \cap \mathcal{C}_i$, which completes the proof. \square

B. Proof of Lemma 3

Proof. (14) can be directly obtained from (12), (2) and (5). Based on the definition of the penalty objective function (2),

$\langle \bar{\mathbf{a}}_i, \nabla B(\boldsymbol{\xi}_{\theta_i}^\gamma, \boldsymbol{\theta}) \rangle \leq 0$ is a linear fractional inequality

$$\langle \bar{\mathbf{a}}_i, \nabla J(\boldsymbol{\xi}_{\theta_i}^\gamma) \rangle + \gamma \frac{1}{-g_\theta(\boldsymbol{\xi}_{\theta_i}^\gamma)} \langle \bar{\mathbf{a}}_i, \nabla g_\theta(\boldsymbol{\xi}_{\theta_i}^\gamma) \rangle \leq 0, \quad (36)$$

with a positive denominator $-g_\theta(\boldsymbol{\xi}_{\theta_i}^\gamma) > 0$ due to (12).

Multiplying the denominator on both side and substituting the weight-feature expression of g_θ in (5) yields $\boldsymbol{\theta}^\top \mathbf{h}_i \leq b_i$ in Lemma 3. The condition $-g_\theta(\boldsymbol{\xi}_{\theta_i}^\gamma) > 0$ itself yields $\boldsymbol{\theta}^\top \boldsymbol{\phi}(\boldsymbol{\xi}_{\theta_i}^\gamma) < -\phi_0(\boldsymbol{\xi}_{\theta_i}^\gamma)$ in Lemma 3.

This completes the proof. \square

C. Proof of Lemma 4

Proof. For any $i = 1, 2, 3, \dots$, the plan $\boldsymbol{\xi}_{\theta_i}^\gamma$ is a solution to the optimization (3), with $\boldsymbol{\theta} = \boldsymbol{\theta}_i$. Recall Lemma 1, $g_{\theta_i}(\boldsymbol{\xi}_{\theta_i}^\gamma) < 0$. Extending the feature-weight expression of $g_{\theta_i}(\boldsymbol{\xi}_{\theta_i}^\gamma)$, one can get $\boldsymbol{\theta}_i^\top \boldsymbol{\phi}(\boldsymbol{\xi}_{\theta_i}^\gamma) < -\phi_0(\boldsymbol{\xi}_{\theta_i}^\gamma)$. Since the optimal solution $\mathbf{u}_{0:T-1}^{\theta_i, \gamma}$ is a minimizer to (3), it means

$$\nabla B(\boldsymbol{\xi}_{\theta_i}^\gamma, \boldsymbol{\theta}_i) = 0. \quad (37)$$

Note that with $g_{\theta_i}(\boldsymbol{\xi}_{\theta_i}^\gamma) < 0$, the above $\nabla B(\boldsymbol{\xi}_{\theta_i}^\gamma, \boldsymbol{\theta}_i)$ is well defined. With (37),

$$\langle \mathbf{a}, \nabla B(\boldsymbol{\xi}_{\theta_i}^\gamma, \boldsymbol{\theta}_i) \rangle = 0, \quad (38)$$

always holds. Extending the above (38) leads to

$$\langle \mathbf{a}, \nabla J(\boldsymbol{\xi}_{\theta_i}^\gamma) \rangle - \gamma \frac{1}{g_{\theta_i}(\boldsymbol{\xi}_{\theta_i}^\gamma)} \langle \mathbf{a}, \nabla g_{\theta_i}(\boldsymbol{\xi}_{\theta_i}^\gamma) \rangle = 0. \quad (39)$$

Due to $-g_{\theta_i}(\boldsymbol{\xi}_{\theta_i}^\gamma) > 0$, one can multiply $-g_{\theta_i}(\boldsymbol{\xi}_{\theta_i}^\gamma)$ on both sides of the above equality, which leads to $\boldsymbol{\theta}_i^\top \mathbf{h}_i = b_i$ based on the definition (15). The second term in (18) directly follows $g_{\theta_i}(\boldsymbol{\xi}_{\theta_i}^\gamma) < 0$. This concludes the proof. \square

D. Proof of Lemma 5

Proof. By Lemma 4, the MVE center $\boldsymbol{\theta}_i = \bar{\mathbf{d}}_{i-1}$ is on the cutting hyperplane $\boldsymbol{\theta}^\top \mathbf{h}_i = b_i$. Directly from [61], one has

$$\frac{\text{Vol}(\Theta_{i-1} \cap \{\boldsymbol{\theta} | \boldsymbol{\theta}^\top \mathbf{h}_i \leq b_i\})}{\text{Vol}(\Theta_{i-1})} \leq 1 - \frac{1}{r}. \quad (40)$$

Since

$$\text{Vol}(\Theta_{i-1} \cap \{\boldsymbol{\theta} | \boldsymbol{\theta}^\top \mathbf{h}_i \leq b_i\}) \geq \text{Vol}(\Theta_{i-1} \cap \mathcal{C}_i) = \text{Vol}(\Theta_i), \quad (41)$$

based on (12), (13), one can get

$$\frac{\text{Vol}(\Theta_i)}{\text{Vol}(\Theta_{i-1})} \leq 1 - \frac{1}{r}, \quad (42)$$

which concludes the proof. \square

E. Proof of Theorem 1

Proof. We complete the proof in two parts. First, we prove the number of learning iterations is less than K , then we use this to prove there will be a $\boldsymbol{\theta}_k \in \bar{\Theta}_H$, $k = 0, 1, 2, \dots, K-1$.

We first prove the total number of iterations must be less than K by contradiction. Suppose the learning iteration number $i \geq K$. With recursively applying lemma 5, one can obtain

$$\text{Vol}(\Theta_i) \leq (1 - \frac{1}{r})^i \text{Vol}(\Theta_0). \quad (43)$$

When $i \geq K$,

$$\text{Vol}(\Theta_i) < \frac{\tau_r \rho_H^r}{\text{Vol}(\Theta_0)} \text{Vol}(\Theta_0) = \tau_r \rho_H^r \leq \text{Vol}(\bar{\Theta}_H) \quad (44)$$

However, from Lemma 2, one has $\bar{\Theta}_H \subset \Theta_i$, meaning $\text{Vol}(\bar{\Theta}_H) \leq \text{Vol}(\Theta_i)$. This leads to a contradiction with (44). Therefore, the total number of iterations must be less than K .

Next, we prove $\exists k < K$ such that $\boldsymbol{\theta}_k \in \bar{\Theta}_H$. In contradiction, suppose $\forall k < K$, $\boldsymbol{\theta}_k \notin \bar{\Theta}_H$. By Lemma 2, this means that for all $i < K$, $\bar{\Theta}_H \subset \mathcal{C}_i$. Then, the algorithm will continue for $i = K$. Consequently, the total number of iterations can reach K , which contradicts that the algorithm will terminate within K iterations. This concludes the proof. \square

F. Proof of Theorem 2

Proof. We complete the proof in two parts. First we prove the algorithm converges to Θ^* which has $\text{Vol}(\Theta^*) = 0$. Based on this, we next prove $\Theta^* \cap \text{int } \Theta_0 = \emptyset$.

We first prove the algorithm converges to Θ^* which has $\text{Vol}(\Theta^*) = 0$. Given the condition $\Theta_0 \cap \bar{\Theta}_H = \emptyset$, the algorithm will never terminate because $\forall i = 1, 2, 3, \dots, \infty$, $\mathcal{C}_i \supset \bar{\Theta}_H$ due to Lemma 2. Since the volume of the initial hypothesis space is finite, by applying Lemma 5 we have

$$\text{Vol}(\Theta^*) = \lim_{i \rightarrow \infty} (1 - \frac{1}{r})^i \text{Vol}(\Theta_0) = 0. \quad (45)$$

Next, we prove $\Theta^* \cap \text{int } \Theta_0 = \emptyset$ by contradiction. Suppose there exists $\boldsymbol{\theta} \in \Theta^* \cap \text{int } \Theta_0$. Define the ball contained in $\bar{\Theta}_H$ to be $\mathcal{B}(\boldsymbol{\theta}_H^c, \rho_H) = \{\boldsymbol{\theta} \mid \|\boldsymbol{\theta} - \boldsymbol{\theta}_H^c\| \leq \rho_H\} \subseteq \bar{\Theta}_H$ with $\boldsymbol{\theta}_H^c$ as the center. By the equation (13), we can note

$$\Theta^* = \Theta_0 \cap \mathcal{C}, \quad (46)$$

with $\mathcal{C} = \bigcap_{i=1}^{\infty} \mathcal{C}_i$ a convex set. So we have

$$\Theta^* \subseteq \mathcal{C}. \quad (47)$$

By equation (12),

$$\mathcal{B}_H \subseteq \bar{\Theta}_H \subseteq \mathcal{C}. \quad (48)$$

From the relationship between sets above, $\boldsymbol{\theta}_H^c \in \mathcal{C}$, $\hat{\boldsymbol{\theta}} \in \mathcal{C}$.

Since $\boldsymbol{\theta}_H^c \notin \Theta_0$, there exists $\mu > 0$ such that

$$\tilde{\boldsymbol{\theta}} = \hat{\boldsymbol{\theta}} + \mu(\boldsymbol{\theta}_H^c - \hat{\boldsymbol{\theta}}) \in \text{int } \Theta_0. \quad (49)$$

Then, one can define a ball $\mathcal{B}(\tilde{\boldsymbol{\theta}}, d)$ centered at $\tilde{\boldsymbol{\theta}}$ with radius

$$d = \min_{\boldsymbol{\theta} \in \text{bd } \Theta_0} \|\tilde{\boldsymbol{\theta}} - \boldsymbol{\theta}\|. \quad (50)$$

Thus, $\mathcal{B}(\tilde{\boldsymbol{\theta}}, d) \subset \text{int } \Theta_0$.

Next, we will show $\mathcal{B}(\tilde{\boldsymbol{\theta}}, \mu \rho_H) \subset \mathcal{C}$. In fact, for any $\boldsymbol{\theta}$ satisfying $\|\boldsymbol{\theta} - \tilde{\boldsymbol{\theta}}\| \leq \mu \rho_H$, one has

$$\begin{aligned} \boldsymbol{\theta} &= \mu \left(\frac{1}{\mu} (\boldsymbol{\theta} - \tilde{\boldsymbol{\theta}}) + \boldsymbol{\theta}_H^c \right) + \tilde{\boldsymbol{\theta}} - \mu \boldsymbol{\theta}_H^c \\ &= \underbrace{\mu \left(\frac{1}{\mu} (\boldsymbol{\theta} - \tilde{\boldsymbol{\theta}}) + \boldsymbol{\theta}_H^c \right)}_{\in \mathcal{B}_H \subseteq \mathcal{C}} + (1 - \mu) \underbrace{\tilde{\boldsymbol{\theta}}}_{\in \Theta^* \subseteq \mathcal{C}}. \end{aligned} \quad (51)$$

The convexity of \mathcal{C} leads to $\boldsymbol{\theta} \in \mathcal{C}$, which means the ball $\mathcal{B}_\mu \triangleq \{\boldsymbol{\theta} \mid \|\tilde{\boldsymbol{\theta}} - \boldsymbol{\theta}\| \leq \mu \rho_H\} \subset \mathcal{C}$.

Let a new ball be $\mathcal{B}(\tilde{\theta}, \min(\mu\rho_H, d))$. Based on the previous two results of $\mathcal{B}(\tilde{\theta}, d) \subset \text{int}\Theta_0$ and $\mathcal{B}(\tilde{\theta}, \mu\rho_H) \subset \mathcal{C}$, one has $\mathcal{B}(\tilde{\theta}, \min(\mu\rho_H, d)) \subset (\Theta_0 \cap \mathcal{C}) = \Theta^*$. As a result,

$$\text{Vol}(\Theta^*) \geq \text{Vol} \mathcal{B}(\tilde{\theta}, \min(\mu\rho_H, d)) > 0 \quad (52)$$

which contradicts $\text{Vol}(\Theta^*) = 0$ from (45). Thus, $\Theta^* \cap \text{int} \Theta_0 = \emptyset$ must hold. This completes the proof. \square

APPENDIX B

SETTINGS OF EXPERIMENTS AND USER STUDIES

A. Inverted Pendulum

In the dynamics of an inverted pendulum (26), the physical parameters is set in Table IV. When the system state violates

TABLE IV
PHYSICS PARAMETERS IN PENDULUM NUMERICAL STUDY

Parameter	Value	Interpretation
m	1kg	Weight of the pendulum
l	1m	Length of the pendulum
g	10m/s ²	Gravitational Acceleration
d	0.1	Dampening Coefficient

$g_{\theta_H}(\xi_\theta^\gamma) \leq 0$ or it is near the target, the pendulum state is uniformly randomly reset between $[0, 0]^\top$ and $[\frac{2\pi}{3}, 3]^\top$. Simulated human correction will continue to be applied until the learned parameters θ_i fall in Θ_H , which terminates one trial.

B. Simulated Quadrotor Navigation

1) *Environment*: The quadrotor starts from $[0.0, 0.0, 5.0]^\top$ [m]. The starting quaternion $\mathbf{q}_{\text{init}} = [1, 0, 0, 0]^\top$. The target is to navigate to the target position $[15.0, 0.0, 10.0]^\top$ [m] within a zigzag tube. The average radius of the tube section is set to be 2.5m.

2) *Learning Neural Features*: We construct the neural feature ϕ using a neural Signed Distance Function (SDF) model trained on synthetic 3D point samples around the tube surface. Each input coordinate (scaled for stability) is first encoded using sinusoidal positional embeddings, then passed through a 5-layer MLP (width 128, ReLU activations). The positional embeddings are skip-connected to the input of the 5th hidden layer. The penultimate layer outputs a 16D feature vector used as ϕ ; the final layer predicts a scalar signed distance supervised during training.

Training data is generated by randomly perturbing surface points on the tube. Signed distance labels are computed as the offset from the nearest point on the tube surface to the sample point, and normals are estimated from the same displacement vector pointing from the nearest surface point to the sample point. The model is trained with three loss terms: L_2 distance loss, cosine similarity loss on normals (via auto-diff), and Eikonal loss to regularize gradient norm, which is similar to the work [62]. Optimization is done using Adam for 250 epochs with a batch size of 1024.

3) *Simulated Correction and Stop Behavior*: Correction signals $\mathbf{a}_x = [-1, 0, 1, 0]^\top$, $\mathbf{a}_y = [0, 1, 0, -1]^\top$, $\mathbf{a}_z = [1, 1, 1, 1]^\top$ in drone control space is used throughout the experiments, corresponding to different motion directions in cartesian space. During the process of learning positional constraints with polynomial features or neural features, if the distance between the quadrotor and the nearest point on the surface of the tube is less than 0.6, a simulated correction \mathbf{a} is applied in the action space of the drone, based on the vector $\mathbf{d} = (d_x, d_y, d_z)$ pointing from the closest tube surface point to the drone position:

$$\mathbf{a} = d_y \mathbf{a}_y + d_z \mathbf{a}_z. \quad (53)$$

Intuitively, the simulated correction "pulls" the drone to the center of the tube (designated safe region). After each correction, the navigation restarts, emulating an emergency stop. During the process of learning velocity constraint, Simulated human corrections against the velocity direction of form:

$$\mathbf{a} = -v_x \mathbf{a}_x - v_y \mathbf{a}_y - v_z \mathbf{a}_z \quad (54)$$

are applied whenever the velocity $\mathbf{v} = (v_x, v_y, v_z)$ exceeds 0.4, and an emergency stop is triggered if it surpasses 0.45.

C. Quadrotor Navigation Game with Real Human Feedback

1) *Environment*: The drone starts from $[0.1, y_{\text{init}}, 0.5]^\top$ with y_{init} uniformly randomly in an interval $[4, 6]$. The starting quaternion $\mathbf{q}_{\text{init}} = [1, 0, 0, 0]^\top$. We set three different targets at positions $[19, 1, 9]^\top$, $[19, 5, 9]^\top$ and $[19, 9, 9]^\top$, with quaternion $[1, 0, 0, 0]^\top$. For the narrow gate (yellow rectangle) in Fig. 16(a), both its size and position are unknown, and one only roughly knows its x position $x_{\text{gate}} \approx 9.8$.

Since the location of the gate is unknown, the drone needs to learn a safety constraint in its safe MPC policy with humans guidance in order to successfully fly through the gate. In the drone MPC policy (1), the dynamics and its parameters are set following [20]; and we generically set the constraint function $g_\theta(\xi)$ using a set of N Gaussian radial basis functions (RBFs)

$$g_\theta(\xi) = \phi_0 + \sum_{i=1}^N \theta_i \phi_i(\xi). \quad (55)$$

As discussed in Section III-C4, we fix $\phi_0 = -1$ to avoid learning ambiguity, and use $N = 20$ temporally accumulated RBFs defined as

$$\phi_i(\xi) = \sum_{t=0}^T \beta_t \text{RBF}_i(\mathbf{x}_t), \quad (56)$$

where β_t is a weighting factor to balance the immediate and future constraint satisfaction. If one emphasizes instant safety, more weights will be given to the initial time step. In our implementation, we choose an exponentially decaying β_t starting at $t = 5$, i.e. $\beta_t = 0, t < 5$ and $\beta_t = 0.9^{t-5}, t \geq 5$ to achieve better predictive safety performance. In (56), each RBF is defined as

$$\text{RBF}_i(\mathbf{x}_t) = \begin{cases} \exp(-\epsilon^2 \|r_{xy,t} - c_{xy,i}\|^2), & i = 1, \dots, 10 \\ \exp(-\epsilon^2 \|r_{xz,t} - c_{xz,i}\|^2), & i = 11, \dots, 20 \end{cases}. \quad (57)$$

Here, the variables $r_{xy,t} = [r_{x,t}, r_{y,t}]^\top$ and $r_{xz,t} = [r_{x,t}, r_{z,t}]^\top$ with r_x, r_y, r_z from \mathbf{x}_t . The i th center $c_{xy,i} = [c_{x,i}, c_{y,i}]^\top$ or

$c_{xz,i} = [c_{x,i}, c_{z,i}]^\top$ is defined with $c_{x,i} = x_{\text{gate}} = 9.8$, $c_{y,i}$ and $c_{z,i}$ are evenly chosen on interval $[0, 10]$. We set $\epsilon = 0.45$. The initial hypothesis space Θ_0 for possible θ in (55) is set as $\mathbf{c}_l = [-80, \dots, -80]^\top$ and $\mathbf{c}_u = [100, \dots, 100]^\top$. γ is 50. This initialization blocks the drone from advancing to the gate at the beginning of the game, leading to conservative behavior in the learning process. The drone will proceed toward the gate after few corrections.

2) *Human Correction Interface*: The drone's motion is visualized in MuJoCo using two complementary camera views: a first-person tracking view and a fixed third-person view. The gate, the current MPC plan, and the target position are always shown to the user. Human users provide corrections through keyboard inputs during flight. Key-command mappings are given in Table V. Whenever a correction is detected, the safety constraint (55) in the MPC policy is updated instantly. Pressing ENTER resets the drone to its initial state and reset the target.

TABLE V
KEYBOARD COMMANDS IN UAV USER STUDY

Key	Correction	Interpretation
"up"	$[-1, 0, 1, 0]^\top$	Go forward (adding positive y-axis torque)
"down"	$[1, 0, -1, 0]^\top$	Go backward (adding negative y-axis torque)
"left"	$[0, 1, 0, -1]^\top$	Go left (adding negative x-axis torque)
"right"	$[0, -1, 0, 1]^\top$	Go right (adding positive x-axis torque)
"shift"	$[1, 1, 1, 1]^\top$	Go up (increasing all thrusts)
"ctrl"	$[-1, 1, 1, 1]^\top$	Go down (decreasing all thrusts)
"enter"	N/A	Reset robot position and switch target.

D. Franka Constrained Reaching Game

1) *Environment*: The arm starts at a configuration in which the end-effector position $\mathbf{r}_{\text{init}} = [0.22, -0.5, 0.48]^\top$ and altitude $\mathbf{q}_{\text{init}} = [0, -0.707, 0, 0.707]^\top$. The reaching target position \mathbf{r}^* will be randomly chosen from three options $[-0.6, -0.5, 0.4]^\top$, $[-0.6, -0.5, 0.5]^\top$, $[-0.6, -0.5, 0.6]^\top$. The reaching target attitude is $\mathbf{q}^* = [0, -0.707, 0, 0.707]^\top$. The slot size and position are unknown except its rough x-position which is $x_{\text{slot}} \approx -0.15$.

We adopt a two-level control scheme, where a safe MPC policy (high-level) is defined for the end effector, which generates the desired velocity for a given low-level operational space controller to track. In the safe MPC policy, we model the end-effector dynamics as

$$\begin{aligned} \dot{\mathbf{r}} &= \mathbf{v}^d, \\ \dot{\mathbf{q}} &= \frac{1}{2} \Omega(R^\top(\mathbf{q})\mathbf{w}^d)\mathbf{q}, \end{aligned} \quad (58)$$

where \mathbf{r} and \mathbf{q} is the position and the quaternion of the arm end-effector in the world frame. $R^\top(\mathbf{q})$ is the rotation matrix from the end-effector frame to the body frame. $\Omega(\cdot)$ is the matrix operator of the angular velocity for quaternion multiplication. Define the robot state and control input

$$\mathbf{x}_t = [\mathbf{r}_t, \mathbf{q}_t] \in \mathbb{R}^7, \quad \mathbf{u}_t = [\mathbf{v}_t^d, \mathbf{w}_t^d] \in \mathbb{R}^6, \quad (59)$$

respectively.

The above end-effector dynamics is discretized with $\Delta t = 0.1$ s. In (1), the MPC horizon is $T = 20$. Let $\mathbf{x}^* = [\mathbf{r}^* \ \mathbf{q}^*]$

denote the target end-effector pose. The step cost $c(\mathbf{x}_t, \mathbf{u}_t)$ and terminal cost $h(\mathbf{x}_T)$ in (1) is set to

$$\begin{aligned} c(\mathbf{x}_t, \mathbf{u}_t) &= (\mathbf{r}_t - \mathbf{r}^*)^\top Q_r (\mathbf{r}_t - \mathbf{r}^*) + k_q \text{diff}(\mathbf{q}_t, \mathbf{q}^*) \\ &\quad + \mathbf{v}_{I,t}^\top R_v \mathbf{v}_{I,t} + \mathbf{w}_{I,t}^\top R_w \mathbf{w}_{I,t}, \\ h(\mathbf{x}_T) &= (\mathbf{r}_T - \mathbf{r}^*)^\top S_r (\mathbf{r}_T - \mathbf{r}^*) + \mu_q \text{diff}(\mathbf{q}_T, \mathbf{q}^*). \end{aligned} \quad (60)$$

In this game, the cost parameters are set as $Q = \text{diag}(2, 2, 2)$, $k_q = 1$, $R_v = \text{diag}(30, 30, 1)$, $R_w = \text{diag}(0.85, 0.85, 0.85)$, $S_r = \text{diag}(80, 80, 80)$, and $\mu_q = 60$. The output of the MPC controller is sent to the low-level controller to track.

TABLE VI
KEYBOARD COMMANDS IN ROBOT ARM USER STUDY

Key	Correction	Interpretation
"left"	$[0, 0, 0, 0, 0, 1]^\top$	Clock-wise rotation of the gripper
"right"	$[0, 0, 0, 0, 0, -1]^\top$	Anti-clock-wise rotation of the gripper
"shift"	$[0, 0, 0, -1, 0, 0]^\top$	Go up in world frame
"ctrl"	$[0, 0, 0, 1, 0, 0]^\top$	Go down in world frame
"Enter"	N/A	Reset robot position and switch target.

Similar to Appendix B-C, to constrain r_z and \mathbf{q} for proper height and tilt in order to pass through the slot. We use a set of $N = 20$ Gaussian radial basis function (RBFs) to parameter the safety constraint:

$$g_\theta(\boldsymbol{\xi}) = \phi_0 + \sum_{i=1}^N \theta_i \phi_i(\boldsymbol{\xi}), \quad (61)$$

with

$$\phi_i(\boldsymbol{\xi}) = \sum_{t=0}^T \beta_t \text{RBF}_i(\mathbf{x}_t), \quad \text{and} \quad (62)$$

$$\text{RBF}_i(\mathbf{x}_t) = \begin{cases} \sigma(r_{x,t}) k_z \exp(-\epsilon_z^2 (r_{z,t} - c_{z,i})^2), & i=1, \dots, 10 \\ \sigma(r_{x,t}) \exp(-\epsilon_q^2 \text{diff}(\mathbf{q}_t, \mathbf{q}_{c,i})), & i=11, \dots, 20 \end{cases} \quad (63)$$

Here, k_z is used to balance the scaling between position and orientation RBFs, $\sigma(r_{x,t})$ is defined as

$$\sigma(r_{x,t}) = \text{sigmoid}(50((r_{x,t} - x_{\text{slot}})^2 - (\frac{w}{2})^2)), \quad (64)$$

which is used to constrain the RBF_i only taking effect around x range $[x_{\text{slot}} - \frac{w}{2}, x_{\text{slot}} + \frac{w}{2}]$ (recall slot's x location, slot, is a approximate value). In the above definition, $w = 0.3$, $k_z = 0.05$, $\epsilon_z = 12$ and $\epsilon_q = 1.8$. The center of positional RBF, $c_{z,i}$, is evenly chosen on interval $[0, 1]$, and the center of orientation RBF, $\mathbf{q}_{c,i}$, is generated by $(\cos \frac{\alpha}{2}, \sin \frac{\alpha}{2}, 0, 0) * \mathbf{q}_{\text{init}}$ with α evenly chosen from $[-\pi/4, 3\pi/4]$ to make sure $\mathbf{q}_{c,i}$ covers all possible orientations. $\beta_t = 0.9^t$ if $t < 5$ and 0 otherwise. The bounds of the initial hypothesis space Θ_0 is set to $\mathbf{c}_l = [-3, \dots, -3]^\top$ and $\mathbf{c}_u = [5, \dots, 5]^\top$. γ is set to 1.5. This initialization leads to a conservative MPC policy, preventing the arm from approaching the target at the beginning.

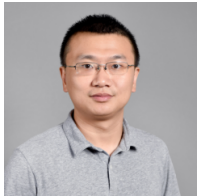
2) *Human Correction Interface*: The robot arm's motion is visualized in MuJoCo using a free-view mode (Fig. 16(b)), allowing users to adjust the camera to a preferred angle. The slot and the randomized reaching target remain visible throughout the task. Users provide corrections to the robot arm via keyboard input, following the specified key-command mappings. Whenever a correction is detected, the safety constraint (61) in the Franka arm's safe MPC policy is updated immediately. Pressing ENTER resets the arm to its initial position and randomizes the reaching target.



Zhixian Xie Zhixian Xie is currently a Ph.D. student in Arizona State University, Tempe, AZ, USA. In 2022, he received B. Eng degree in automation at Shanghai Jiaotong University, Shanghai, China. His research focuses mainly on controls, robotic learning from human and robot dexterous manipulation.



Wanxin Jin Wanxin Jin is an assistant professor the School for Engineering of Matter, Transport and Energy at Arizona State University (ASU). Previously, he was a postdoctoral fellow at the GRASP Laboratory at the University of Pennsylvania. He obtained his doctorate from Purdue University in 2021. His research includes robotics, control and machine learning, with a focus on the autonomy of robots interacting with humans and objects.

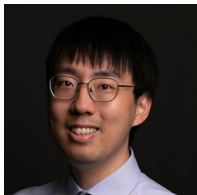


Wenlong Zhang Wenlong Zhang is an associate professor in the School of Manufacturing Systems and Networks at Arizona State University, where he serves as the Research Director. He is a core faculty member in the Robotics and Autonomous Systems and Systems Engineering PhD programs. He joined ASU faculty in 2015 after earning his doctoral degree in mechanical engineering from the University of California, Berkeley. At ASU, he leads the Robotics and Intelligent Systems Laboratory (RISE Lab), and teaches undergraduate- and graduate-level classes on

dynamics, control systems, optimization, and robotics.



Yi Ren Yi (Max) Ren is an associate professor of aerospace and mechanical engineering in the School for Engineering of Matter, Transport and Energy at Arizona State University. he directs the Design Informatics Laboratory at ASU. His group studies computational and data-driven methods that will augment or transform the activities of engineering and industrial design. Ren's current research interests include optimization, product/configuration design, human-computer interaction and machine learning.



Zhaoran Wang Zhaoran Wang is an associate professor with Northwestern University, working at the interface of machine learning, statistics, and optimization. He is the recipient of the AISTATS (Artificial Intelligence and Statistics Conference) notable paper award, ASA (American Statistical Association) best student paper in statistical learning and data mining, INFORMS (Institute for Operations Research and the Management Sciences) best student paper finalist in data mining, Microsoft PhD Fellowship, SimonsBerkeley/J.P. Morgan AI Research Fellowship, Amazon Machine Learning Research Award, and NSF CAREER Award.

Amazon Machine Learning Research Award, and NSF CAREER Award.



George J. Pappas George J. Pappas is the UPS Foundation Professor at the Department of Electrical and Systems Engineering at the University of Pennsylvania. He also holds a secondary appointment in the Departments of Computer and Information Sciences, and Mechanical Engineering and Applied Mechanics. Previously, he served as the Deputy Dean for Research in the School of Engineering and Applied Science. Pappas's research interest focus on control systems, robotics and autonomous systems, formal methods, machine learning for safe and secure

cyber-physical systems. He has received numerous awards including the NSF PECASE, the Antonio Ruberti Young Researcher Prize, the George S. Axelby Award, the O. Hugo Schuck Best Paper Award, and the George H. Heilmeier Faculty Excellence Award. Pappas has mentored more than fifty students and postdocs, now faculty in leading universities worldwide. He is a Fellow of IEEE, IFAC, and was elected to the National Academy of Engineering in 2024.